Università degli Studi di Cagliari

DOTTORATO DI RICERCA IN FISICA

Ciclo XXVIII

Synthesis and Characterization of Bi_2S_3 Colloidal Nanoparticles for Photovoltaic Applications

Settore/i scientifico disciplinari di afferenza

SSD FIS/03, CHIM/03

Presentata da: **Roberto Piras**

Coordinatore Dottorato: **Prof. Alessandro De Falco**

Tutor / Relatore: **Prof. Michele Saba**, **Prof.ssa Anna Musinu**

Esame finale anno accademico 2014 – 2015

UNIVERSITÀ DEGLI STUDI DI CAGLIARI

SCUOLA DI DOTTORATO DI FISICA

FIS/03, CHIM/03

Ciclo XXVIII

Synthesis and Characterization of Bi_2S_3 Colloidal Nanoparticles for Photovoltaic Applications

Supervisors:	**PhD Student:**
Prof. Michele Saba	**Roberto Piras**
Prof. Anna Musinu	

Ph.D. School Coordinator:
Prof. Alessandro De Falco

Final exam, academic year

2014-2015

Unione Europea
Fondo Sociale Europeo

Repubblica Italiana

REGIONE AUTONOMA
DELLA SARDEGNA

FSE 2007-2013
POR
SARDEGNA
obiettivo competitività regionale e occupazione

Abstract

Global energy consumption is expected to increase significantly together with the greenhouse gas emissions and the problem of fossil fuels exhaustion. Solar energy, as an alternative and renewable form of energy, has gained popularity as possible solution for all these problems. Lots of materials have been studied to implement the energy conversion efficiency of the so-called third generation solar cells. These devices could be a cheaper alternatives to the silicon-based ones. Unfortunately, they are often characterized by short lifetime or health hazardous materials. Bismuth sulfide (Bi_2S_3) is a promising n-type semiconductor for solar energy conversion. In this work, the properties of the compound will be discussed, as well as its potential for applications in solar energy technology. We have explored the colloidal synthesis of Bi_2S_3 nanocrystals, with the aim of employing them in the fabrication of solution-processable solar cells and to replace toxic heavy metals chalcogenides like PbS or CdS, that are currently employed in such devices.

We compare different methods to obtain Bi_2S_3 colloidal quantum dots, including the use of environmentally benign reactants, through organometallic synthesis. Surfactant-assisted colloidal synthesis (SACS) methods were used to synthesize Bi_2S_3 nanoparticles with different size and shape. These methods have been employed changing systematically several parameters such as temperature and time of synthesis, concentration of chemical reagents and sulfur precursors. Morphological characteristics and optical properties of all

the synthesized nanoparticles have been characterized by X-ray diffraction (XRD), transmission electron microscopy (TEM), Fourier transform infrared spectroscopy (FT-IR), UV-Vis and photoluminescence (PL) spectroscopy.

After the characterization of electrical properties of bismuth sulfide samples together with the preliminary attempts to find the most advantageous methods for the production of homogeneous film on conductive supports, a sample was chosen like standard and it was employed in building of various prototype of third generation solution processed solar cells. Dip and spin coating techniques were employed to produce homogeneous film of nanoparticles on conductive support, also in combination with organic polymer such P3HT, Pedot:PSS and Spiro-OMeTAD. The resulting solar cells were tested for power conversion efficiency (PCE).

Synthesis and characterizations have been carried out in Dipartimento di Scienze Chimiche e Geologiche, Università degli Studi di Cagliari, under the supervision of Prof. Anna Musinu and Prof. Carla Cannas. Optoelectronic characterizations and solar cells manufacturing have been carried out in Dipartimento di Fisica, Università degli Studi di Cagliari, under the supervision of Prof. Michele Saba, Prof. Andrea Mura and Prof. Giovanni Bongiovanni.

Roberto Piras gratefully acknowledges Sardinia Regional Government for the financial support of his PhD scholarship (P.O.R. Sardegna F.S.E. Operational Programme of the Autonomous Region of Sardinia, European Social Fund 2007-2013 - Axis IV Human Resources, Objective l.3, Line of Activity l.3.1.)

Contents

Chapter 1

Introduction

World energy demand is growing constantly because of the continuous technological progress. However, the current energy sources might not be enough for the next future. As visible in Fig. 1.1, in 40 years the energy consumption has more than doubled[1]. Latest predictions speculate that this demand will increase by 37% by 2040 with an annual growth of 2%, reduced to 1% from 2025[2].

The main energy sources used currently are fossil fuels (FFs) which meet around 82% of the world energy demand (Fig. 1.2)[1]; this category includes coal, oil and natural gas. While the coal consumption has been almost constant, oil and natural gas demand has increased together with the electricity need. These raw materials are used to produce plastic materials but mainly they are converted into other energy forms. They are burned to produce heat for our houses, to cook and other necessity or burned to convert heat into mechanical work, often used to produce electricity. The FFs are diffused on Earth but finite and not renewable. According with the peak oil Hubbert theory[3], which concerns the temporal evolution of resources exploitation, oil and natural gas lifetime has been estimated to be around 50-60 years. This means that, at the current rate, the FFs sources could run out by 2070[4].

Each combustion process, independently from the application, produces water and carbon dioxide (CO_2); this last one has a primary role in the greenhouse effect linked to the global warming and so to the climatic changes. Greenhouse gases accumulate in the upper atmosphere and prevent heat release to the space, increasing the average temperature at the ground. This phenomenon is very important because it contributes to the maintenance of the life on Earth. Unfortunately an excess of greenhouse gases causes a progressive increasing of the temperature. This fact influences several factors of the terrestrial ecosystem, causing climatic changes always more evident from satellite pictures and detections done by NASA's orbital satellites. Sea level and global temperature rising, oceans warming and acidification, ice sheets shrinking, Arctic sea ice declining and extreme weather events are all attributed to the global warming[5]. In particular, it has been demonstrated that CO_2 atmospheric level grows up and decrease with cycles of hundreds thousands years, maintaining its average level stable. However, after the industrial revolution the CO_2 level started to grow up over the maximum levels ever reached in the past and it never stopped, breaking the natural cycle[6,7].

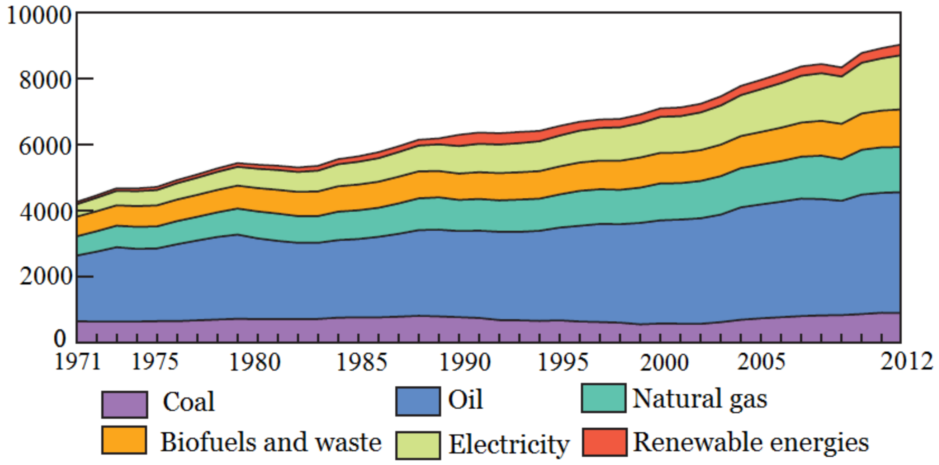

Fig. 1.1: World consumption from 1971 to 2012 by fuel expressed as million tons of oil equivalent (Mtoe). Picture adapted from International Energy Agency 2014 report[1].

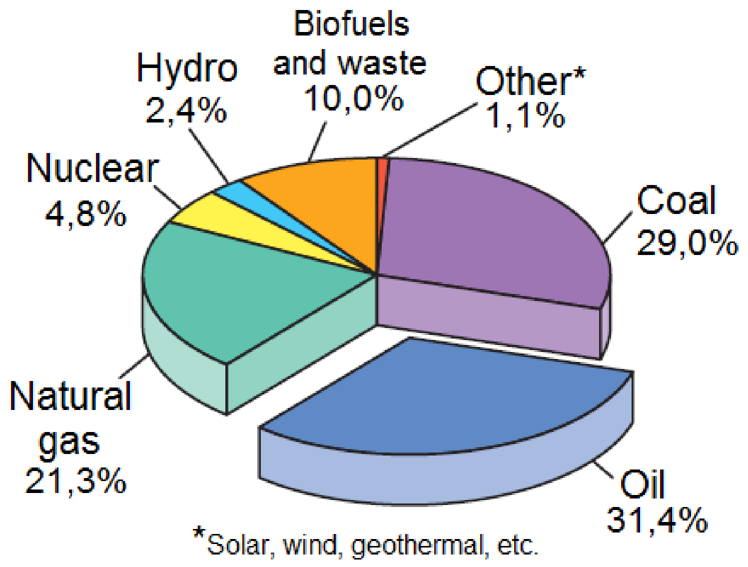

Fig. 1.2: World energy supply in 2012. Picture adapted from International Energy Agency 2014 report[1].

The research of a solution for the energy issue has increased in the latest decades. To find sources which will not produce greenhouse gases, ways to stock the CO_2 in excess and use it to produce something else useful could be all good alternatives. However, to trap and stock the CO_2 from the atmosphere or directly during the combustion could postpone the problem but not solve it, except if the collected CO_2 will be used to produce other organic compounds; in this way, this issue would be turned into a resource. Recently a two steps CO_2 and H_2O electrochemical conversion method has been tested to produce ethanol, useable as bio-fuel[8].

1.1 Renewable energies

Looking for alternatives to FFs, lots of research groups have focused their efforts to the so-called renewable energies (REs). For the human lifetime point of view, in fact, natural sources are endless. The Sun, the wind, the flowing water, the biomass and the Earth's internal heat all belong into this category. The real problem is to find a way to use them efficiently. At the moment, focusing on their use to produce electric power, REs need expensive investments. The comparison between different energy sources is not easy and we must consider that to obtain electricity might be needed several energy conversion steps. Data reported in Table 1.1, show the U.S. levelized energy costs (LEC) versus the energy source used. LEC represents the cost of a power plant, based on a given energy source, over its life divided to the sum of electricity produced over the same lifetime. This parameter does not consider state incentives or retail prices. FFs appears most convenient than REs despite their environmental impact. Other RE sources, like geothermal or hydro, seem advantageous but they have also strong limits. Wind could be a reasonable option because it could be present all day long, for all the years. However it is intermittent, stronger

Source of energy	Cost($/kWh)
Coal	$ 0.10-0.14
Natural Gas	$ 0.07-0.13
Nuclear	$ 0.10
Solar PV	$ 0.13
Solar Thermal	$0.24
Hydro	$ 0.08
Wind	$ 0.08-0.20
Geothermal	$ 0.05
Biomass	$ 0.10

Table 1.1: US LEC for different energy sources[9].

or weaker as function of the weather and, to exploit totally its potential, the wind turbines must be distant from each other and so occupy a wide area[10]. Similar observations can be done also for geothermal, hydro and biomass that need large area to produce a power energy amount comparable with the FFs or solar ones. The Sun is also an intermittent source, due to the day/night cycle, but the power generated and the develop of the dedicated devices make this the most promising alternative to FFs use. The initial investment is more expensive than FFs one but, with the progressive consumption of these resources and the growing interest of global governments to reduce CO_2 emissions, the price is bound to decrease; for the same reason, FFs cost is bound to rise.

1.1.1 Solar energy

Solar light can be used to produce both thermal and electrical energy. Devices which allow the conversion of light in these energy forms are called “solar panels” and can be divided into two categories: solar thermal panel and solar photovoltaic panel. Solar thermal panels use solar light to heat a fluid and to drive the heat for purposes from domestic heating to electricity production. Some systems are designed in order to concentrate the light using specific mirrors, to increase the efficiency of the device. Solar photovoltaic panels, instead, produce electricity thanks to chemical-physics properties of the semiconductors from which they are made. Each panel is composed by a variable number of cells (solar cells) which are responsible of the photo-conversion.

Currently, the photovoltaic devices are divided into three “generations”. The first generation includes the first prototypes based on crystalline silicon and used in monocrystalline or polycrystalline panels. The second generation includes amorphous silicon-based panels and photovoltaic modules made using thin film technologies. All cells based on different materials and approaches to convert the energy belong to the third generation. This one includes cells built with organic polymers, multi-junction cells (concentrator photovoltaic), quantum dots-based and hybrid solar cell. These last two categories are correlated because built using nanostructured semiconductor.

Basically, a photovoltaic device is formed by semiconductor materials, so its operation mode is strongly correlated to their bandgap, regardless whether they are organic or inorganic. These materials are enclosed between two electrodes, often conductive glass. If the photon energy is sufficiently higher than the semiconductor bandgap, an electron can be promoted from the valence band to the conduction band. Consequently, a hole is created in the valence band. Electron and hole move to opposite electrodes, allowing the current flow. Silicon-based solar cells are usually formed by two silicon layers, one n-type doped and the other one p-type doped. Third generation solar cells are based on the same principles but replacing completely the silicon with organic polymers and dyes or with other inorganic semiconductors. Organic dye-based cell, as Grätzel solar cells, have approached average power conversion efficiencies of the silicon-based cells[11,12]. Dye and iodine electrolyte solution play the role of active materials and they allow a fair control on bandgap, simply changing the dye used. These devices are cheap to manufacture, lightweight, both stiff and flexible[12,13]. Unfortunately, for the organic nature of the dye and the liquid state of the electrolyte, these cells have quite short lifetime, making them not really competitive for commercial purposes. For this reason, it is became important to find an alternative to these unstable components which could allows similar or better control on bandgap energy levels.

1.2 Nanomaterial semiconductors

IUPAC defines nanomaterials as “particle of any shape with dimensions in the 1x10^{-9} and 1x10^{-7} m range”[14]. So all the materials, especially for solid crystalline state, with at least one of their dimension in this range belong to this category and they could be classified as nano-plates (only one dimension into the nano range), nano-wires (two nano-dimensions) and nano-particles (three nano-dimensions). The 100 nm limit is due to the fact that, under this dimension range, novel properties characterize these materials, particularly concerning the optoelectronic field; this phenomenon is called quantum size effect (QSE). Nanocrystal semiconductors, called also quantum dots, are the example which best represents this phenomenon.

They are aggregate of a given number of atoms with a well defined crystalline lattice that shows different properties if compared with their same bulk crystal. Imaging a particle into a 3D potential well, after the necessary calculation, it is possible to find a correlation between the particle energy and the reverse of the squared diameter (L) of the well. The same consideration can be done for an electron into a nanoparticle as visible in Eq.(1.1), where the value L is the radius of the spherical nanoparticle studied and m_e is the electron effective mass. Quantum size effect acts also on the continuous band energy of the bulk material that becomes discrete in the quantum dot. The smaller is the nanoparticle radius, the higher will be the difference in energy between valence band and conduction band, changing progressively the optical and electronic properties of the material.

$$E_g^{QDots} \approx E_g^{Bulk} + \frac{\hbar^2\pi^2}{2m_eL^2} \tag{1.1}$$

The possibility to tune the bandgap is very important in the photovoltaic field; it means to have the control on the spectral range of the optical radiation that can be absorbed by the material. The larger is this range, the better the solar energy could be exploited without waste but with some limits. Materials with small band-gap can absorb a broad portion of the spectrum but the solar cell based on them will not work because of a too low open-circuit voltage. Instead, high band-gap energy materials could generate an advantageous voltage value but unfortunately they do not absorb the low energy wavelengths of the spectrum and so the number of charge carriers generated will be poor, reducing consequently the density of current. This relationship between energy gap and voltage has been shown in 1960 by Shockley and Queisser, who have also defined the optimal band-gap value for a single junction photovoltaic cell around 1,4 eV[15,16].

At the same time, the high percentage of atoms on the surface, compared to the number of core atoms, makes these particles often very reactive particularly when exposed to air. Very stable semiconductor materials that could be directly synthesized into nano-range dimensions are the heavy metal chalcogenides, that is to say the compounds formed by the reaction between a dense metal with the 6A group elements of the periodic table, also known as chalcogens, except for oxygen whose compounds are called oxides. Compounds as

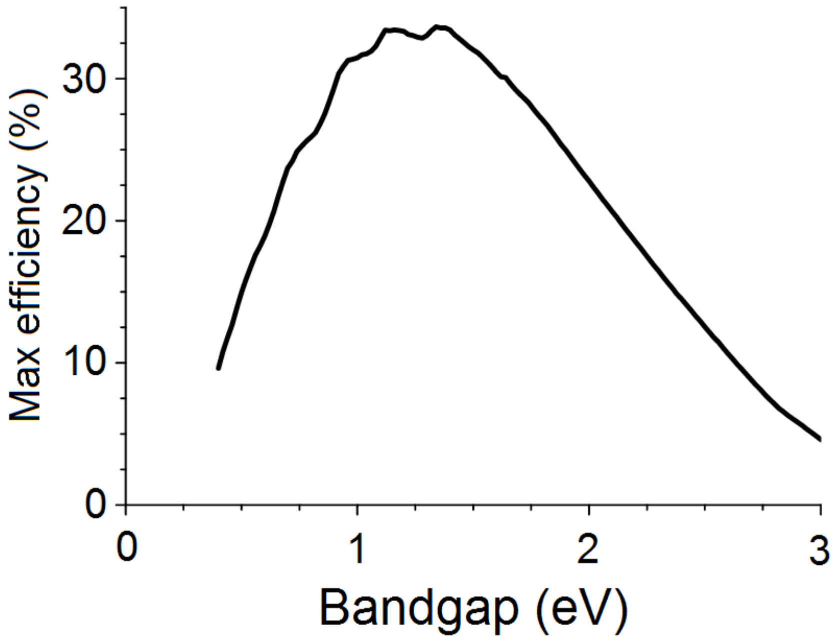

Fig. 1.3: Shockley-Queisser limit for the efficiency of a solar cell.
(Source: https://en.wikipedia.org/wiki/Shockley%E2%80%93Queisser_limit)

lead sulfide (PbS) or cadmium sulfide or selenide (CdS, CdSe) are often used as example for their appreciable results in the photovoltaic field and for their optical properties[17–19]. However they also present some health hazards because of the heavy metal on their formula. Lead and cadmium are in fact very dangerous for the health of people if inhaled or swallowed. These heavy metals affect especially the nervous system, gastrointestinal tract and the blood but can also give cancer in other organs; their effect increase when taken in organic salt form[20,21]. For this reason, environmentally benign nanocrystals are currently a very central topic in materials research for solar energy conversion[22–26]. On the other hand, not all these materials are so toxic after all. PbS, for example, has a so high stability that also whether the release of Pb^{2+} ion has been demonstrated, their amount is too low to make serious damages to the organism. This means that pollution risk and danger for the human health actually would derive from the industrial activities, the chemical precursors used and accidents, therefore limited to workers and the environment near to the factories. Despite this, the PbS is commonly considered toxic. It is so necessary to find an alternative that could reconcile the technological expectation of the scientist with the public opinion.

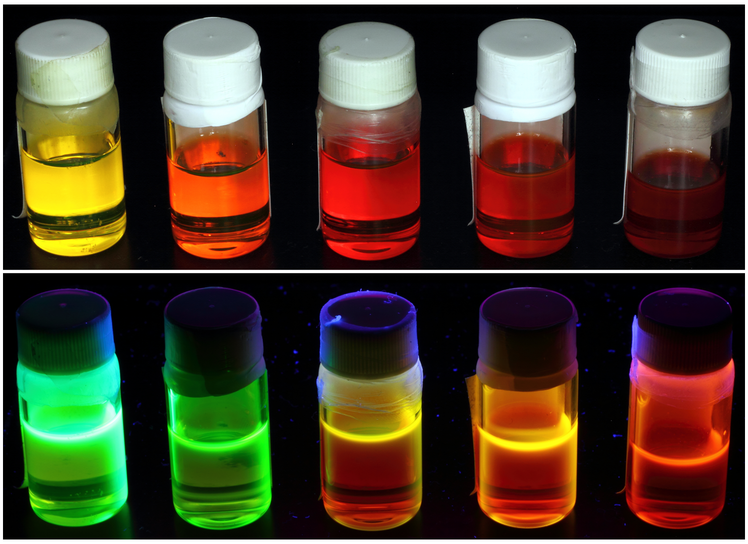

Fig. 1.4: CdSe colloidal solutions under visible (up) and UV (down) illumination. Particles with different diameter show different color and photoluminescence.

1.2.1 Bismuth sulfide

Bismuth sulfide (Bi_2S_3) belongs to the class of non-toxic semiconductor materials that can be studied for this aim. Bismuth is a non toxic heavy metal and its sulfide is also non toxic. In fact, a distinctive feature of this material is its biocompatibility[27,28] that allows the use of Bi_2S_3 for environmentally friendly devices or in biomedicine[29]. Another distinguishing property is the strong anisotropic crystal structure, consisting of weakly interacting one-dimensional ribbons, made by tightly bonded [Bi_4S_6] units in an herring-bone arrangement[30–32] (Fig. 1.5). Bi_2S_3 is also an important material for optoelectronics because of its large optical absorption coefficient (10^{-4} cm^{-1})[33] as well as its small direct band gap (reported in literature between 1,3 and 1,8 eV[34–42]), features that make it ideal in photodetector devices[43] and as sensitizer or electron acceptor in photovoltaics[16,44–46]. Contrary to PbS, Bi_2S_3 shows an n-type character and it has been demonstrated that a large fraction of optically excited electrons relax down to conduction band states while holes are quickly captured by midgap states[30]. In fact, a well-known defect in bulk Bi_2S_3 is the sulfur vacancies that, for the presence of dangling bonds, can produce relaxation effect on the surface, and so the midgap traps[30,47]. Obviously, in the nano range, this fact acquires high relevance and it becomes important to passivate the atoms on the surface.

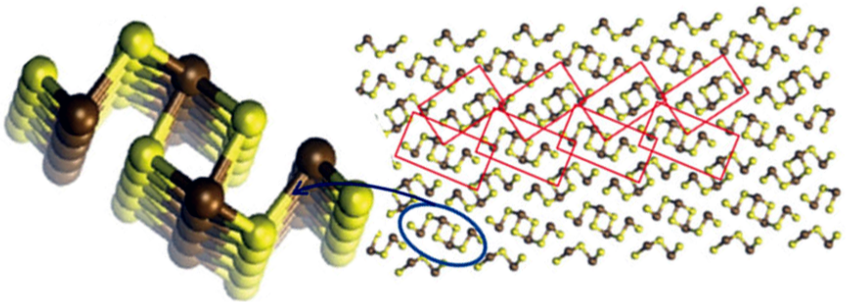

Fig. 1.5: Crystal structure of Bi_2S_3 (S atoms in yellow, Bi atoms in brown). In red is highlighted the herringbone pattern of ribbons (magnified on left). Nano-ribbons grow perpendicularly to the plane, long the [001] direction.

Several synthesis approaches have been proposed to improve the control of nanocrystal size and shape[48–53]. Bi_2S_3 has been synthesized by a variety of techniques such as chemical bath deposition[54], solvothermal[55] and colloidal methods[30,43,49,52,56] in several shapes, including dots[22,30,57], nanorods[30,50,58], nanowires[49,58,59], flowers[58,60,61] and nanotubes[33]. Often these morphologies exceed the “100 nm limit” at least for one dimension, except for the nanoparticles synthesized by colloidal methods which seems to allow a better size control. Moreover the colloidal synthesis performed with long chain surfactants produce always nanoparticles covered by organic molecules layers which drives the growth of the particles during the synthesis and it could also passivated their surface.

1.3 Aim of the thesis

In this thesis I will describe my experimental work concerning the synthesis, characterization and application of Bi_2S_3 nanoparticles for development of third generation solution processed solar cells.

In Chapter 2, I will describe all the surfactant-assisted colloidal synthesis (SACS) methods used to synthesize Bi_2S_3 nanoparticles with different size and shape. These methods have been employed changing systematically several parameters such as temperature and time of synthesis, concentration of chemical reagents and sulfur precursors. The chapter also reports all the characterization performed on each samples using X-ray diffraction (XRD), transmission electron microscopy (TEM), Fourier transform infrared spectroscopy (FT-IR), UV-Vis and photoluminescence (PL) spectroscopy in order to study morphological characteristics and optical properties of the nanoparticles synthesized.

In Chapter 3, I will describe building steps of solar cell prototypes based on Bi_2S_3 nanoparticles. The characterization of electrical properties of bismuth sulfide samples shown in the previous chapter are reported together with the preliminary attempts to find the most advantageous methods for the production of homogeneous film on conductive supports. Then, I will describe the development of the solar cell prototypes built with bilayer and bulk heterojunction architectures. Cell parameters are also reported for each prototype tested.

Chapter 2

Colloidal bismuth sulfide nanocrystals

Bismuth sulfide was synthesized using variants of “surfactant-assisted colloidal synthesis” method (SACS), which consists in two steps: nucleation and growth. A mixture of metallic precursor and one or more surfactants in organic high-boiling solvents is heated usually under inert atmosphere to avoid the reaction of metal cations with the atmospheric oxygen. At a certain temperature the nucleation step starts, wherein the precursor decomposes forming an aggregate of few atoms, called nucleus, which bond together and with the surfactants in dynamic equilibrium. Nuclei become thermodynamically stable only after a certain critical size, after which they can only grow. Surfactants act as stabilizer, driving the particles growth towards a particular thermodynamic state, promoting a certain geometry rather than another. With the advance of the growth step, the particles can incorporate smaller nuclei (Ostwald ripening) or form clusters. The final product is a dispersion of nanoparticles maintained colloidally stable into the organic solvent through a surfactant layer that covers their surface; this layer is commonly called “organic capping” while the dispersion is called “colloidal solution”.

Nucleation and growth are not separate steps causing often a large nanoparticles size distribution. However, the growth kinetics is conditioned strongly by the temperature. The choice of a given metallic precursor which decomposes at relatively low temperature helps to define the beginning of the nucleation step. Another method, called "hot injection" (HJ), is based on the injection of precursors directly to the hot solvent to obtain their faster decomposition and so a faster nucleation. This method is useful to prevent nuclei formation during the growth of other particles already formed. Increasing the temperature, the kinetic energy of the system increases, promoting faster addition of other atoms on the surface nucleus; these atoms are driven by the dynamic equilibrium between bonded and not bonded surfactant on the surface. In this way, the nucleation step can be distinguished by the growth step, giving a better control on the morphology of the final product.

An oleic acid-based SACS with HJ method was used to synthesize Bi_2S_3 colloidal nanocrystals. All the syntheses tested began heating a mixture of a bismuth precursor with one or more surfactants in high-boiling organic solvent. The heat decomposes the bismuth precursor, releasing Bi^{3+} cations which form a new compound with the surfactants molecules. Then, a sulfur precursor was fastly injected into the hot bath to originate a fast nucleation of Bi_2S_3. Different growth temperatures were tested to study the differences of size, shape and morphology potentially produced.

The bismuth precursor used for all the syntheses tested was bismuth acetate, an organic salt. For the purpose to find non toxic alternatives to the chalcogenides semiconductor currently used in third generation solar cells, different sulfur precursors have been tested, being the bismuth compounds naturally safe. The first precursor tested was the hexamethyldisilathiane (HMS)[22,43,62]. This compound was chosen for its high reactivity and the affinity with heavy metals to produce their chalcogenides. It was used in combination with oleic acid as surfactant and 1-octadecene as solvent. However the HMS is dangerous if handled without caution, particularly when exposed to air. For this reason, it was also tested sulfur powder as alternative precursor. It was solubilized in different solvents to allow their reactivity with the bismuth precursor. Initially, the S powder was solubilized into 1-octadecene, the same solvent used before, to replace eventually only the HMS into the original method. Sulfur is not soluble at room temperature into this solvent, so high temperatures were necessary to prepare it. However, we found that it is more soluble into a surfactant, the oleylamine, also at room temperature. This new solution could modify drastically the reaction because the introduction of a new surfactant means to modify the dynamic equilibrium on the nuclei surface and so the kinetic which allows their growth and defines their geometry. This S solution was tested in similar condition to the HMS synthesis but with different stoichiometric Bi/S ratio to investigate the crystallographic and optoelectronic influence of a different ion concentration on the final products. Lastly, basing on the results obtained with the HMS and S powder-based synthesis, the effects of the use of oleylamine as only surfactant were studied. Interesting perspectives have emerged from the developing of ultrathin nanowires grown long a crystallographic direction which could allow better conduction properties[47], as detailed below.

In the following, all synthesis methods used are reported. Names were chosen to be representative of the whole reaction and to show the principal differences with respect of the first method tried.

2.1 Colloidal Bi_2S_3 synthesis methods

2.1.1 HMS method

The first method tested was the HMS-method, so called because the sulfur precursor was the hexamethyldisilathiane (a.k.a. HMS). It is mostly based on the method proposed by Konstantatos et al.[22,43]. Bismuth(III) acetate (Ac.Bi), oleic acid (OA) and HMS were used as reactants and 1-octadecene (ODE) was employed as solvent. Some parameters, such injection temperature and reaction time, have been made to change. In a three necks flask, a mixture of 6,4 mmol of Ac.Bi (Aldrich >99%), 13,8 mL of OA (Aldrich 90%) and 13,4 mL of ODE (Aldrich 90%) was heated under stirring in argon atmosphere at 90°C for 16 hrs and then heated up to 170°C. A solution of 9,6 mmol of HMS (Sigma Aldrich, synthesis grade) in 10 mL of ODE was quickly injected into the flask at the same temperature (170°C) or after cooled down at 100°C or at 50°C. After 30 min, 2 or 6 hrs, the solution was quickly cooled down at room temperature adding 20 ml of cold methanol. Successive dispersion/reprecipitation and centrifugation steps were performed to purify the nanoparticles. Finally the sample was dispersed in anhydrous toluene[22,30,43].

2.1.2 ODE method

This synthesis is similar to the HMS method except for the sulfur precursor, that is a solution of elemental sulfur in powder, heated at 100°C for 20 min and then at 180°C for 1 h in ODE[30,43,63]. The dispersion is not stable.

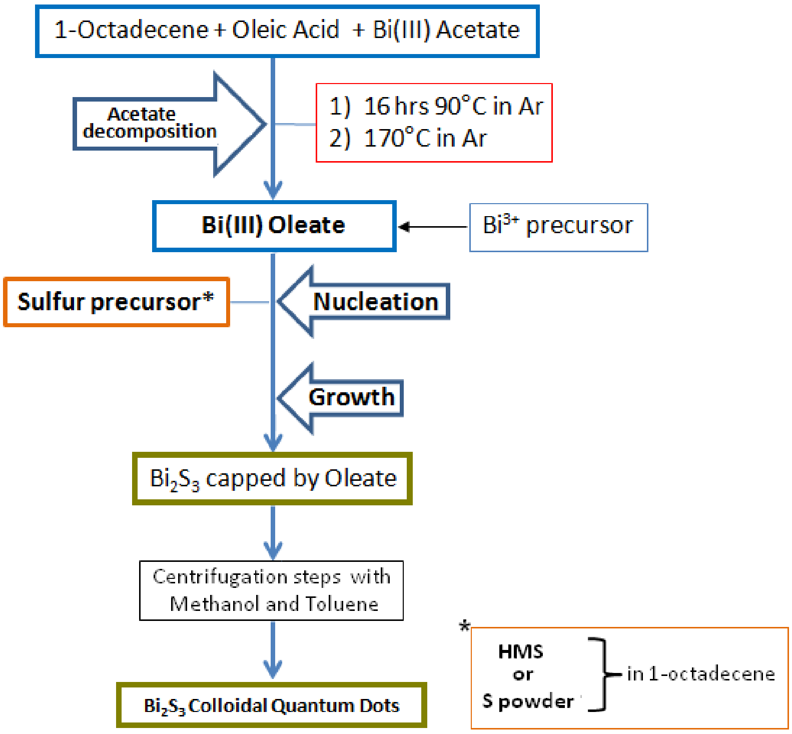

Fig. 2.1: Block diagram of HMS and ODE synthesis methods.

2.1.3 OAm method

OAm method is based on the one propose by Ibañez et al.[52] changing the stoichiometry of the reactant and/or the temperature of sulfur precursor injection. Moreover, the sulfur precursor is elemental sulfur powder dissolved in oleylamine (OAm). This method was tested using the same growth temperature for all sample, different reaction times and different stoichiometric ratios. A mixture of 0,64 mmol of Ac.Bi, 5 ml of OA and 20 ml of ODE was heated under stirring in vacuum at 90°C for 30 min, to obtain a clear solution. Then, in Ar atmosphere, the temperature was increased. Once reached 170°C, 2 ml of a solution elemental sulfur in OAm 0,47 M (0,94 mmol) were quickly injected into the flask. This one was produced stirring strongly the mixture at room temperature, until a red clear solution was obtained. The solution into the flask turned quickly in a black/brown color. After 10, 30 min or 6 hrs at the same temperature, the reaction was quenched and the products cooled down adding 20 ml of cold ethanol. The nanoparticles were purified by two dispersion/reprecipitation and centrifugation steps in toluene/ethanol and finally dispersed in anhydrous toluene[52,64]. These dispersions are colloidally stable for weeks or, sometimes, for months.

This method was tested in:

- Bi/S stoichiometric ratio (StS), with the amount of Bi and S precursor reported above in the text;
- excess of sulfur (ExS), with 0,26 mmol of Ac.Bi and 2 ml of S in OAm 0,47 M (0,94 mmol);
- in defect of sulfur (DfS), with 3,2 mmol of Ac.Bi and 2 ml of S in OAm 0,47 M (0,94 mmol).

The StS was tried also injecting only 0.8 ml of the S solution with 0,26 mmol of Ac.Bi to see if, reducing OAm with respect of OA, the crystallinity will increase or decrease.

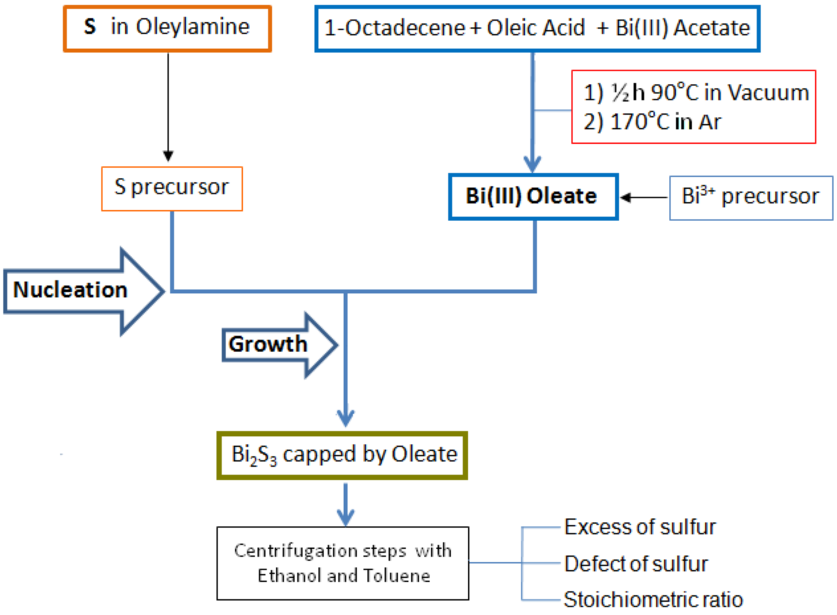

Fig. 2.2: Block diagram of OAm synthesis methods.

2.1.4 NW method

NW method is based on the bismuth sulfide necklace nanowires synthesis proposed by Cademartiri et al.[49,65] and it is similar to the "OAm" one except for the fact that ODE and OA mixture was replaced by oleylamine. The "NW" name come from the nanowire shape of the final product. A mixture of 3,2 mmol of Ac.Bi and 4,2 ml of OAm was stirred and heated to 130°C over the course of 30 min and then kept at the same temperature for 30 min under Ar atmosphere. 10 ml of S in OAm solution 1,5 M (made as in OAm method) was quickly injected into the flask. After 30 min at 100°C the reaction was quenched with cold toluene. Unsolubilized materials were removed by centrifugation, and acetone was added to the supernatant until it became turbid. The final mixture was centrifuged, the supernatant discarded and the precipitated nanocrystals redispersed in toluene several time until the supernatant became clear. At the end, the particles were dispersed in toluene[47,49,65]. This dispersion is fairly stable with a little deposition of particles on the bottom of its flask.

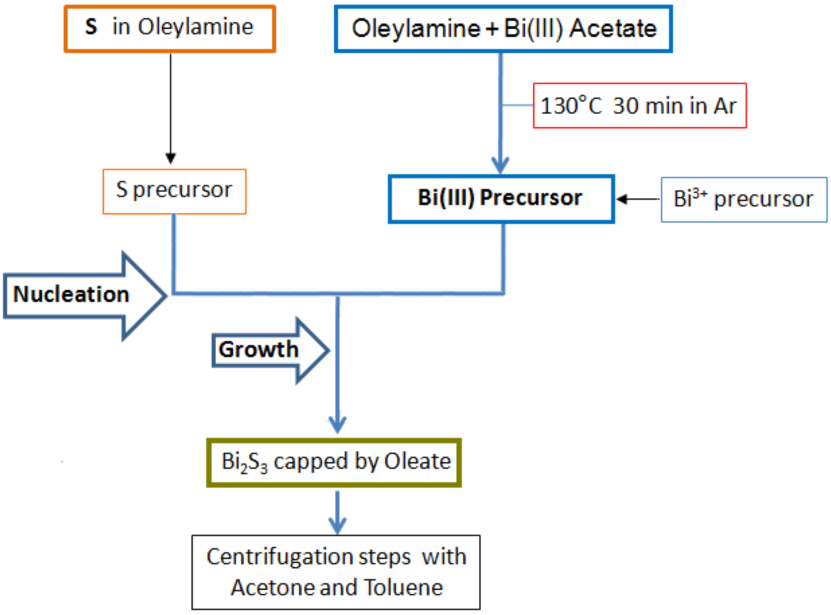

Fig. 2.3: Block diagram of NW synthesis method.

2.2 Morphological and optical characterization

Any synthesis method described were characterized by different capping agents and/or sulfur precursors. Changing one of this parameters at times affects and modifies the growth of nanoparticles, acting on their morphology and size. The synthesis products were characterized by X-Ray powder diffraction (XRD), transmission electron microscopy (TEM), Fourier transform infrared spectroscopy (FT-IR) and UV-Visible absorption spectroscopy (UV-Vis). These characterizations give us information, in the order, about crystalline lattice, size, shape, organic coating, absorption properties and energy of the band-gap of the material. The following sections report the results obtained from all of them.

2.2.1 Morphological characterization

Structural and morphological characterizations of all the samples were performed through XRD and TEM analysis. For XRD analysis, all samples were dried in air from colloidal suspensions and deposited on a silicon crystal sample holder or directly dropped and dried on it. XRD patterns shown in the following chapters were recorded on a Seifert X3000 powder diffractometer with a θ-θ Bragg-Brentano geometry with Cu Kα wavelength. A quantitative evaluation of nanocrystal sizes through the XRD patterns was achieved by a Rietveld refinement procedure using the MAUD software[66].

Highly diluted samples, dispersed in toluene by ultrasonic bath, were dropped on a copper grid covered with a carbon thin film for electron microscopy observations. Micrographs were obtained by a transmission electron microscope (JEOL 200CX) operating at 200 kV. High resolution images were obtained by a JEM 2010-UHR equipped with a Gatan Imaging Filter (GIF) with a 15 eV window and a 794 slow scan CCD camera. Nanoparticles size distribution were calculated measuring the diameters of the particle, or major and minor axis when not spherical, by "ImageJ" software. Then, these values were reported graphically, and their frequency counts were fitted with log-normal function by "Origin" software. The median is used as reference for the average dimensions of the nanoparticles with its standard deviation in brackets as percentage value. Scale bar in the picture were draw using "Adobe Photoshop" software.

All syntheses are reproducible and the same characterizations were performed on any reaction products, in the same condition. Most representative XRD patterns are reported below. Several TEM pictures were collected from at least two batch of the same sample. All syntheses, performed with the same conditions, did not show considerable differences in term of size and morphology of particles produced.

Bi_2S_3 - HMS

The XRD pattern shows a pure sample of orthorhombic Bi_2S_3. Using the PDF-Card n. 17-320 as reference, we note that all signals are respected, with particular attention to the characteristic triplet of bismuth sulfide. The intensity of the peaks is characteristic of the high crystallinity of the material and their widths are attributable to the nanosize of the particles. In Fig. 2.4, the HMS-sample pattern is compared with the commercial Bi_2S_3 powder one. The sample used as reference for the following analysis is the one synthesized at 170°C for 6 hrs.

Fig. 2.5 shows a comparison between the pattern of this sample with the ones obtained changing the temperature of synthesis. Lowering the synthesis temperature causes the widening of the peaks with also a consequent overlap of them. This trend is confirmed by Rietveld refinement of the XRD data. For the sample synthesized at 170°C the best fit was obtained introducing a small microstrain and using a large B_j value (isotropic thermal factor) associated to structural disorder. Lattice parameters (a = 1,114, b = 1,129, c = 0,3985 nm) are in good agreement with crystallographic data. The fitted parameters ($<D>_{XRD}$ of the minor and major axes of nanocrystals), are reported in Table 2.1 together with the final R_w (weighed pattern agreement index). The evolution of the mean crystallite size with the synthesis temperature are also reported. The values obtained by the fit evidence that the decrease of the temperature from 170°C to 100°C and 50°C are in favor of the formation of an increasing number of isotropic single crystals. However, if in the refinement procedure of the sample obtained at 100°C a small contribution (about 8%) related to anisotropic nanocrystal is introduced, a decrease of the $R_w\%$ index by 13,9 down to a value of 8,8 is obtained, suggesting the possible presence of a low fraction of nanocrystalline rods. The reaction temperature represents therefore the key parameter in order to tune the Bi_2S_3 crystallite size.

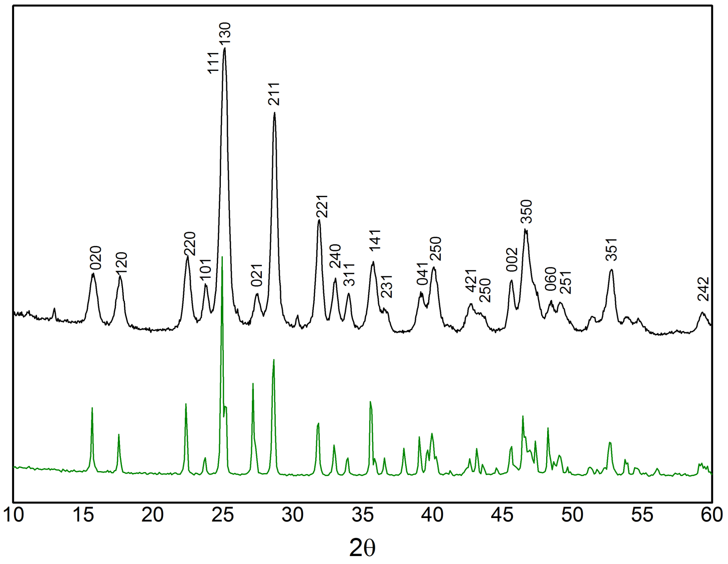

Fig. 2.4: Comparison between HMS-sample (black) and Bi_2S_3 commercial powder (green) patterns. Indexing of the peaks was made using the PDF-Card 17-0320 as reference.

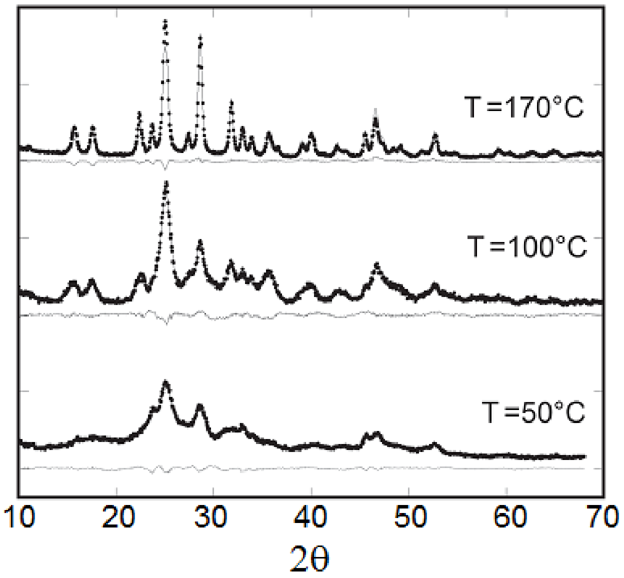

Fig. 2.5: XRD patterns of the samples obtained at 6 hrs for different reaction temperatures (points) with Rietveld simulations (continuous) and residuals. Picture adapted from Aresti et al., Adv. Funct. Mater. 2014[30]

Transmission electron microscopy (TEM) reveals that the HMS sample

Reaction temperature (°C)	Major Axis $<D>_{XRD}$ (nm)	Minor Axis $<D>_{XRD}$ (nm)	Agreement Index R_w (%)	Major Axis $<D>_{TEM}$ (nm)	Minor Axis $<D>_{TEM}$ (nm)
170	26,1 (5)	9,0 (5)	8,8	25 (10)	13 (13)
100	-	8,7 (5)	13,9	29 (14)	14 (19)
50	-	4,5 (3)	7,5	-	3,6

Table 2.1: Average crystallite size evaluated by Rietveld Analysis of XRD patterns with respective agreement index R_w(%). Average particle size calculated by the size distributions reported in Fig. 2.6. All samples have been collected after 6 hrs of growth. Numbers into round brackets represents the percent standard deviation of the given value.

tends to self assemble in a monolayer on the TEM grid, as visible in Fig. 2.6. This sample changes its morphology as a function of the temperature of reaction. If synthesized at 50°C the nanoparticles have as spherical shape with an average diameter of 3,6 nm, but their distribution is also characterized by a long tail extending to 13 nm. At 100°C the shape changes from pure spherical to rod shaped nanoparticles, with average length of 29 nm (14%) and width of 14 nm (19%). The same shape characterizes the sample at 170°C with similar dimension but with a smaller average value. The brightness showed in dark field mode image for any sample is a further proof that are crystalline nanoparticles and, most important, that they are single crystals. These observations are in agreement with those derived from XRD analysis, confirming the presence of nanorods.

These samples also shows an interesting texture, visible in Fig. 2.7, that is a further proof of its crystalline structure common to $(Pn_4Ch_6)n$ pnictide chalcogenides (Pn = Bi, Sb; Ch = S, Se)[30,32]. The orthorhombic bismuth sulfide is formed by assembling of atomic ribbons, made by Bi_4S_6 units periodically assembled. In the picture, it is visible the herring-bone arrangement of these nanoribbons in the same plane. The elements in the ribbon are strongly bonded together and any ribbon bonds each other by Van der Waals bonds.

The growth direction of the nanoribbons, perpendicular of this plane, is the [001][30,32].

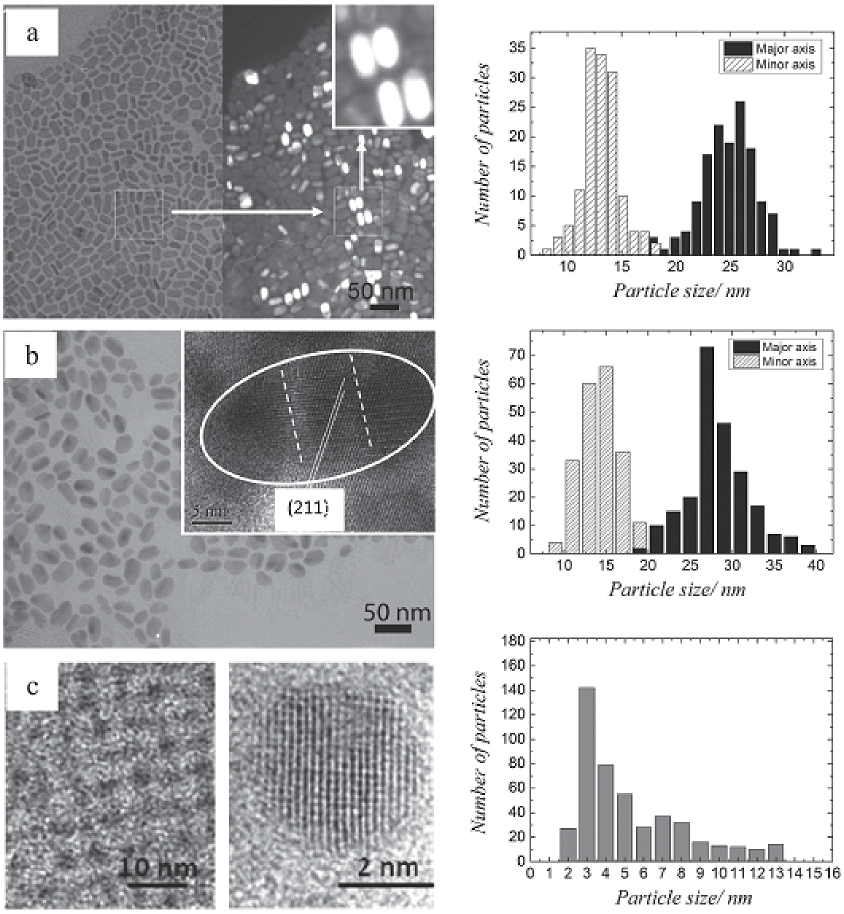

Fig. 2.6: (a) TEM bright and dark field images of HMS sample synthesized at 170°C. (b) Bright field image of HMS sample synthesized at 100°C with high resolution TEM image (inset). (c) High-resolution transmission electron microscopy (HR-TEM) images of the HMS sample synthesized at 50°C. In the right side are reported the corresponding particle size distributions calculated by bright field images. For the 170°C and 100°C samples the size distribution of the minor and major axes of the nanorods are reported. Picture adapted from Aresti et al., Adv. Funct. Mater. 2014[30].

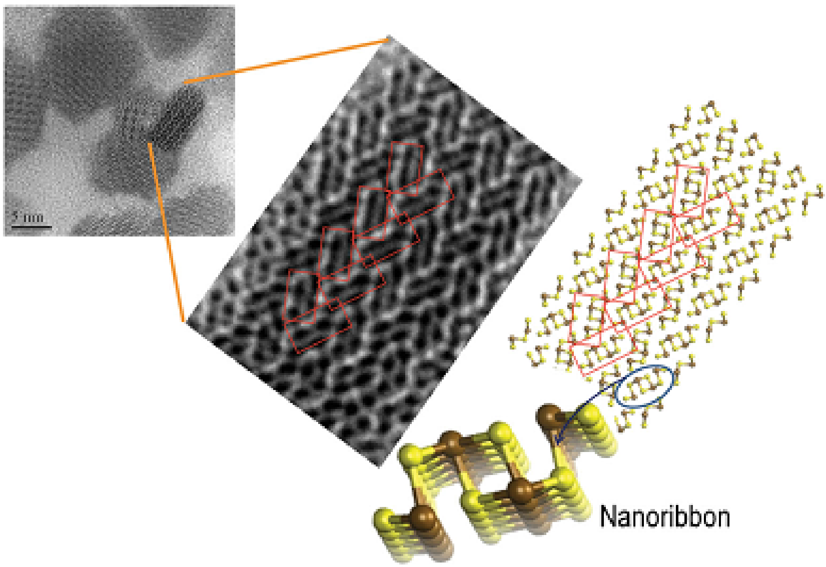

Fig. 2.7: HR-TEM image of Bi_2S_3 nanocrystals. The orthorhombic crystal structure is formed by the assembling of atomic ribbons. In the nanocrystal shown in the enlarged image, the nanoribbon axis is along the [001] crystallographic direction and perpendicular to the figure plane. Ribbons are arranged in a herring-bone motif, as highlighted by the red rectangles. Picture adapted from Aresti et al., Adv. Funct. Mater. 2014[30].

Bi_2S_3 - ODE

Below 170℃ it was impossible to obtain a crystalline phase. From 170℃ onwards the number of signal increases with the temperature. This sample results to be formed by orthorhombic Bi_2S_3 but the pattern shows also a bulge that decrease in intensity with the rising of the temperature, so with an increasing of the particles crystallinity. This could indicate the presence of amorphous phases or very small nanoparticles. Signals at 28,5° and 45°2θ have seen their intensity to increase, suggesting a preferential orientation of the growth along the corresponding crystallographic direction, respectively [211] and [002]. However, a non spherical shape for the particles is expected due to the strong decline of the peak intensity at 27,1°2θ with respect to the reference card, already observed on the HMS-sample patterns. The narrowness of all peaks is also distinctive of not so small particles but even in the nano range; it is so possible to suppose the presence of a double distribution of particles. More information have been obtained through TEM observations.

TEM images reveal that the ODE-sample is very different with respect of the HMS-sample. It has a petal-like appearance, formed by several needles. With the increasing of the growth time, these bundles open their terminals like a flower and show better all the needles. This phenomenon has been reported in literature for similar synthesis methods[26]. The nanoparticles easily exceed 200 nm in length until over 400 nm for the 210℃ sample. In this one, the width can also exceed the 100 nm instead of the tens of nanometers reached at lower temperature. Together with the larger ones, other smaller nanoparticles are visible, smaller than 3 nm, joined in a fiber-like arrangement around the main nanoparticles. It is plausible to think that they are formed first during the nucleation phase and then, through the Ostwald ripening mechanism, they form the main needle-like particles.

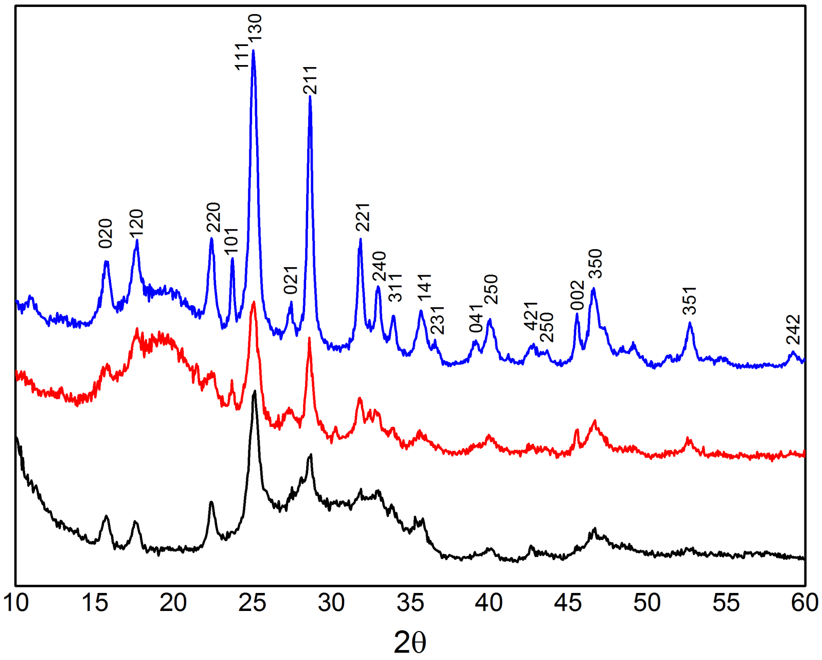

Fig. 2.8: XRD patterns of ODE-samples obtained at 2 hrs with different synthesis temperatures: 170℃ (black), 190℃ (red), 210℃ (blue).

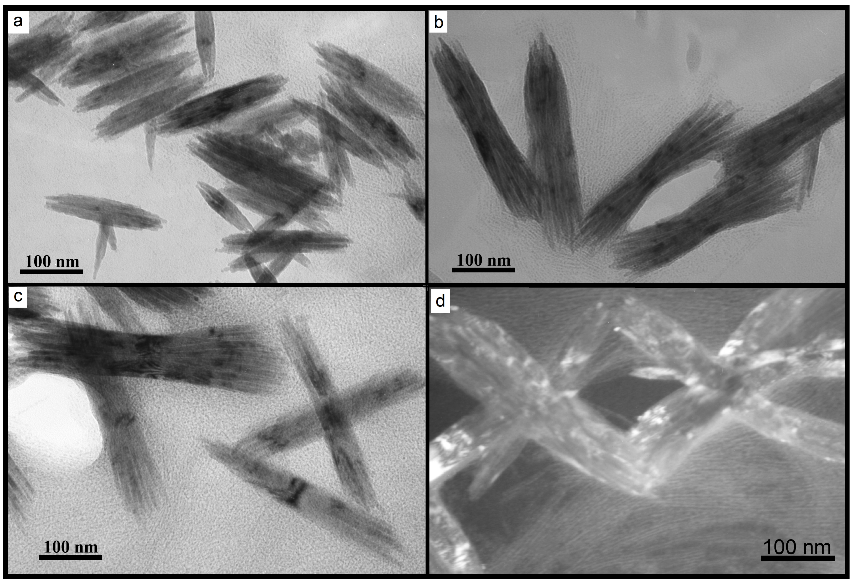

Fig. 2.9: TEM bright field images of ODE sample synthesized at (a) 170℃, (b) 190℃ and (c) 210℃. (d) TEM dark field image of 210℃ sample.

Bi_2S_3 - OAm

This method has been tested changing growth temperature, growth time and also stoichiometric parameters. For this reason, from now on I will refer to samples obtained with a stoichiometric ratio between Bi and S as StS-sample, with excess of sulfur as ExS-sample and with defect of sulfur (so in excess of bismuth) as ExB-sample.

Fig. 2.10 shows the most representative XRD pattern of these samples produced at the same temperature. Bragg reflections indicate that orthorhombic structure is always present but with differences of signal intensities. Peaks look wider than the commercial Bi_2S_3 powder pattern, as expected from nanoparticles. The increased width causes neighboring peaks to overlap. For this reason, we cannot distinguish the singular peak over the 35°2θ. For all samples, it is possible to note the disappearance of the signals at 27,1°, 37,9°, 47,3° and 48,2°2θ corresponding respectively at [021], [041], [530], [060] crystallographic planes. Other signals are not visible in the ExB sample. At the same time, other peaks increase their intensity if compared with the other signals, such as at 28,6° and 45,5° in the ExS sample; this last signal can be present also in the ExB and StS patterns but, increasing the number of washing steps at the end of the synthesis, it loses intensity until its disappearance. At the beginning, this signal was the only narrow one of the patterns. The quality of these patterns does not allow a Rietveld refinement in agreement with the TEM observations because of their noise, the overlap of signals and mostly for the not spherical shape, as visible below. For this reason, information about the size of the particles have been obtained exclusively from the TEM observations.

Studying individually the effects of the others parameters on the synthesis, maintaining the given Bi/S ratio constant, it is easy to note a general increasing of the signal intensity and also their narrowing with the time of reaction. This is not surprising because it is a typical consequence of SACS syntheses.

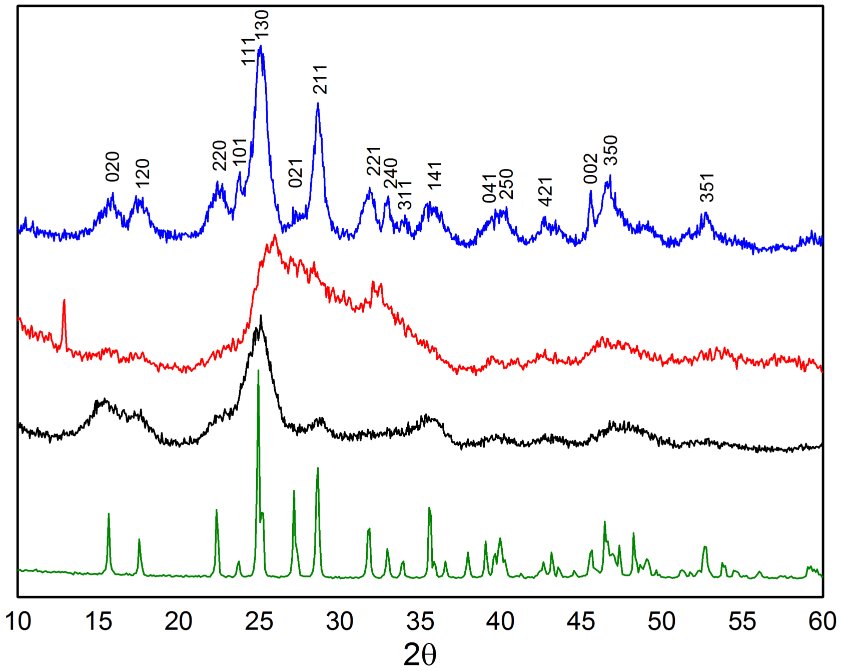

Fig. 2.10: XRD patterns of OAm-samples obtained at 170°C and a reaction time of 30 min with an excess of sulfur (blue), defect of sulfur (red) and stoichiometric Bi:S ratio (black) compared with the commercial Bi_2S_3 pattern (green).

For all samples, 10 min are not enough for a good crystalline growth. After 30 min the patterns exhibit more peaks so the samples are increasing their crystallinity; reached 6 hrs, some peaks show a further increment of intensity but the nanoparticles lose their stability in organic solvent.

StS-sample, initially amorphous, slowly increases its crystallinity with time and this is visible in its pattern characterized by few large signals (Fig. 2.11). Reducing the amount of OAm injected into the flask during the synthesis, so putting more OA in the reaction bath, crystallinity and number of peaks increase. Its patterns show a preferential growth of the signal at different time. In particular, between 30 min and 6 hrs of reaction the [101], [211] and [002] are subjected to great increasing of intensity. Unfortunately, this sample was always colloidally unstable.

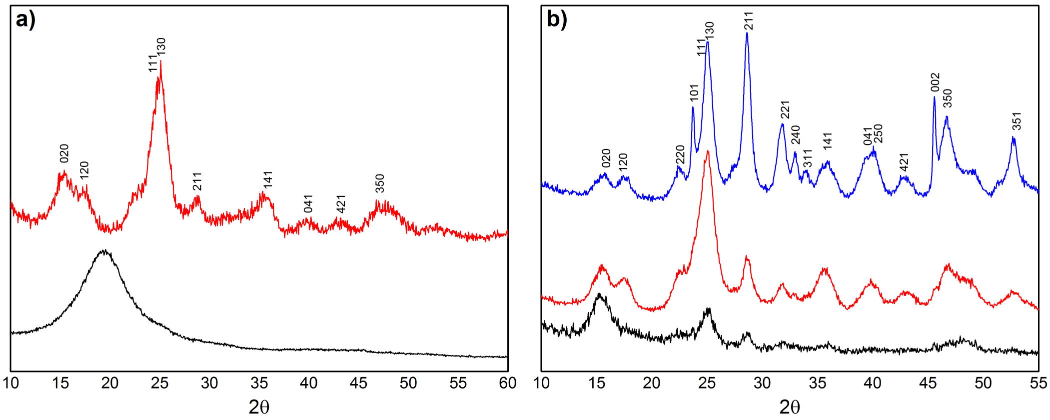

Fig. 2.11: XRD patterns of OAm-samples synthesized (a) with stoichiometric Bi:S ratio and (b) in the same way but with a defect of OAm, at 170°C and at different time of growth: 10 min (black), 30 min (red) and 6 hrs (blue).

Fig. 2.12 shows the StS-sample. It is formed by rod-shaped nanoparticles, both aggregated randomly and organized as bundles of tens of rods with different length, adjacent between them; these bundles can exceed the 600 nm of length. The formation of aggregates makes difficult a good evaluation of sample dimensions and also it is not a good introduction for a material wanted to be used to produce films on substrate by coating deposition methods. The rods have average length of 49,8 nm (17%) and average width of 8,5 nm (4%). Moreover, some nanoparticles in the bundles appear in the picture with darker edge than core; this is commonly associated to different of thickness and it is also a common feature of nanotubes. Unfortunately, the blurring effect due to the organic capping does not allow good enough resolution for magnified pictures and so it is not clear which is the true morphology.

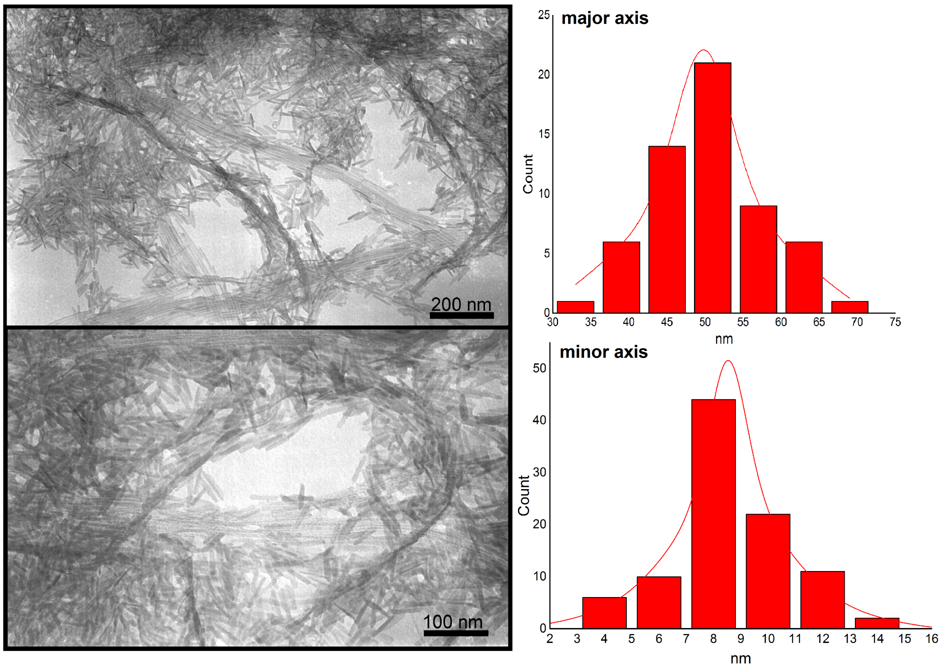

Fig. 2.12: TEM bright field images of StS-OAm sample synthesized at 170°C for 30 min of growth. In the right side are reported the corresponding particle size distributions calculated by these images.

ExB-sample does not show a good crystallinity even increasing the reaction time. The peaks look very large and it is difficult to recognize a crystalline phase on its. At the same time, the large band seems to follow the profile of the Bi_2S_3 pattern and no other crystallographic phase of bismuth sulfide, oxide or sulfate finds a match with it. So, it is reasonable to conclude that the sample could be formed by very small nanoparticles, maybe with a distorted lattice due to the higher concentration of Bi^{3+} during the synthesis.

Fig. 2.14 shows the ExB sample, that has some similarities with the StS sample. Nanoparticles are aggregated, making very difficult to define their dimensions. For the blurring effect due to the capping, it was not possible to collect pictures with higher magnification. Nanoparticles look arranged in two parallel rows but this could also derive to differences of thickness in the same particle and so to a nanotubes morphology. Particles with similar dimension and morphology of the StS sample are also visible.

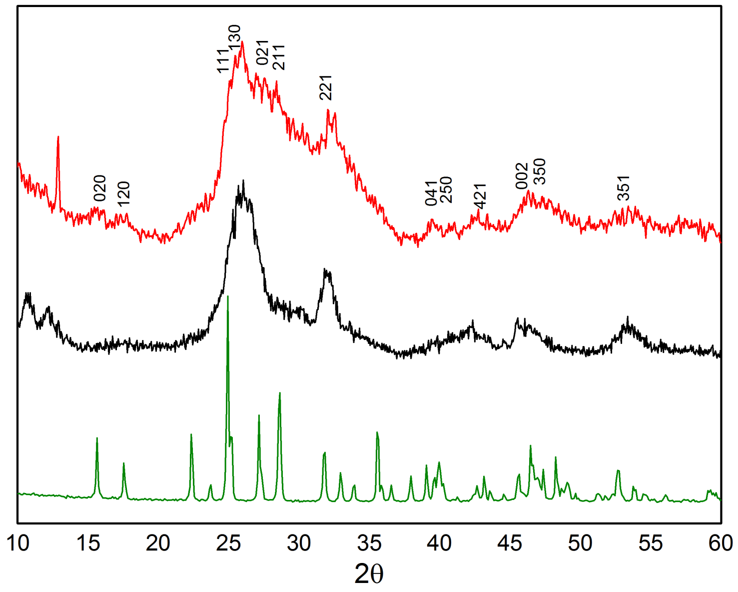

Fig. 2.13: XRD patterns of OAm-samples in excess of Bi, obtained at 170℃ at different time of growth, 10 min (black) and 30 min (red), compared with the Bi_2S_3 commercial pattern (green).

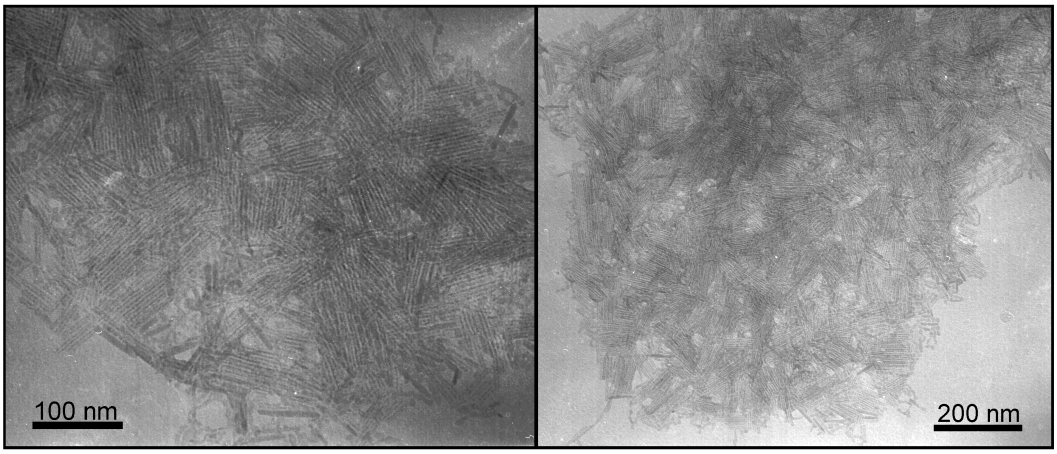

Fig. 2.14: TEM bright field images of ExB-OAm sample synthesized at 170℃ for 30 min of growth.

ExS-sample seems to be the one with the best quality among samples obtained with OAm method. Its pattern is also the most similar to HMS one, especially after 30 min of growth, although is visible a different preferential growth; this fact has been confirmed by TEM observations.

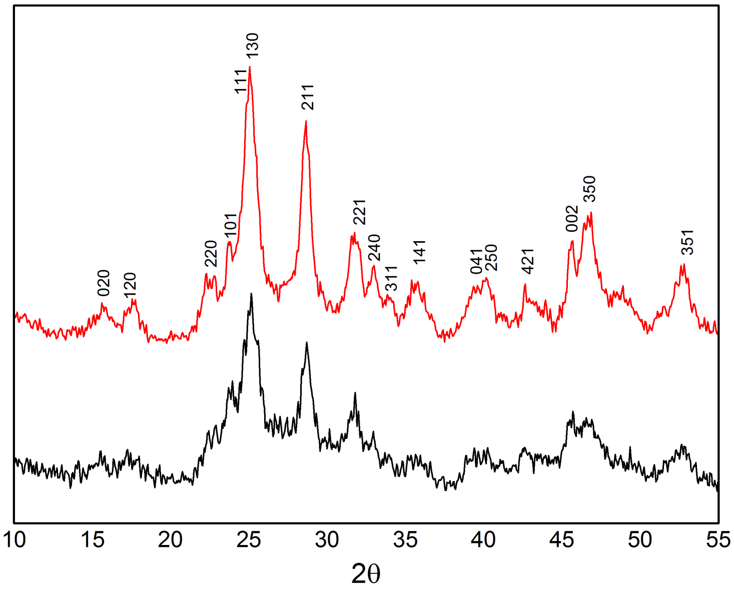

Fig. 2.15: XRD patterns of OAm-samples in excess of S, obtained at 170°C at different time of growth, 10 min (black) and 30 min (red).

Fig. 2.16 shows the ExS sample. This is formed by nanoparticles with rod shape, without a regular distribution observed on the TEM image. After only 1 minute of growth, rod-shape nanoparticles are formed, mainly amorphous. After 10 minutes the nanoparticles become crystalline, with a rod shape and average length of 27 nm (30%) and 6,3 nm (18%) of width. This distribution is also characterized by the presence of a long discontinuous tail extended up to 80 nm, that could be considered like a second distribution but unfortunately the number of counts is not large enough to confirm such second distribution on statistical grounds. All collected pictures show also the presence of monolayer of small particles and particle aggregates. The aggregates are the dominant component in the 30 min grown sample. The average width is 8,5 nm (20%), but with a higher average length of 45 nm (26%) and, most important, without secondary distributions. Dark field images confirm the monocrystallinity of this sample.

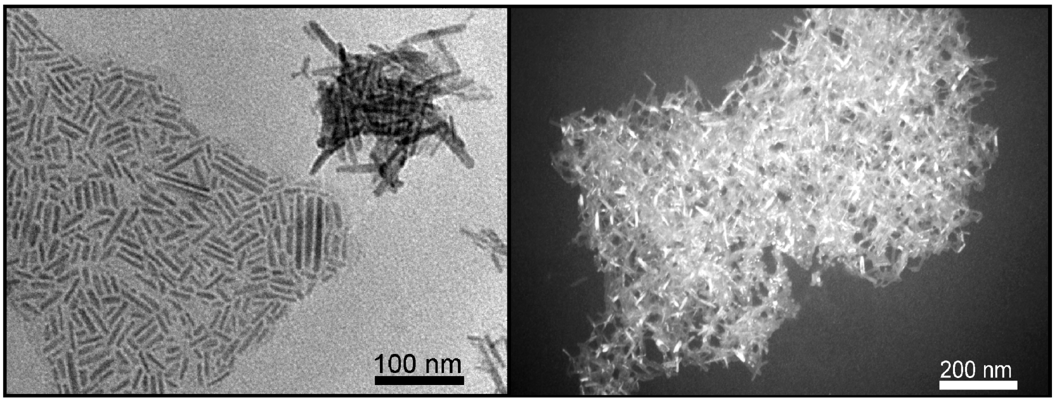

Fig. 2.16: (a) TEM bright field images of ExS-OAm sample synthesized at 170°C for 10 min. (b) Dark field image of ExS-OAm sample synthesized at 170°C for 30 min.

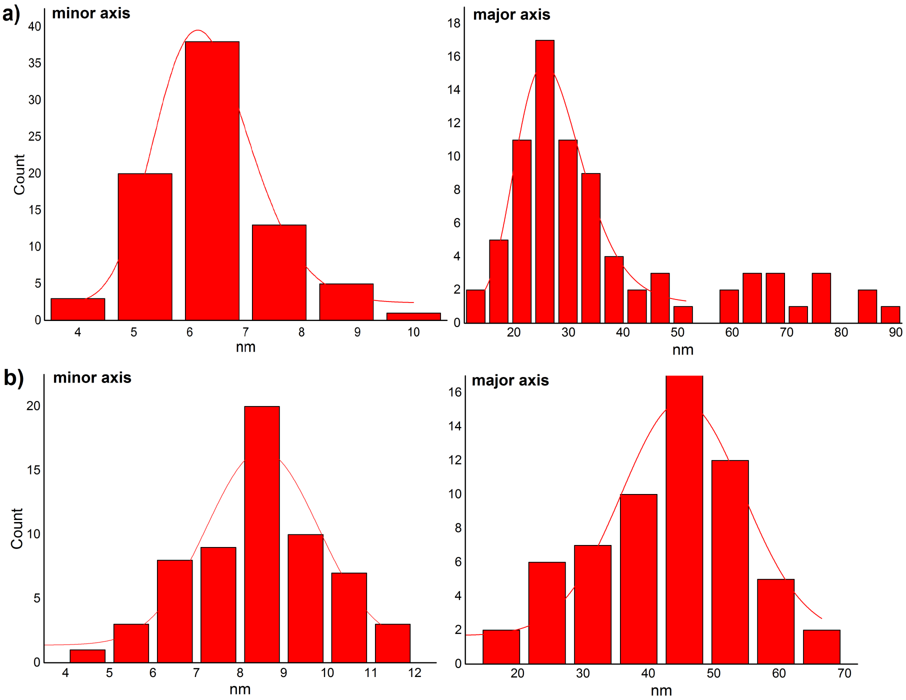

Fig. 2.17: Length and width distribution of ExS-OAm sample after (a) 10 min and (b) 30 min of growth.

Bi_2S_3 - NW

In Fig. 2.18 is shown the XRD pattern of this sample compared with a bismuth sulfide pattern of nanowires produced following the original method[49]. Both of them shown a bulge, usually visible in very small or amorphous nanoparticles, but in the NW one are present also several narrow peaks attributable at the Bi_2S_3 orthorhombic phase (PDF-Card 17-320). Only the first and the second peak are actually unknown; they are probably due to an arrangement of the nanoparticles in a self assembled pattern or to an excess of organic phase. From this comparison it is possible to suppose that the NW-sample is formed by two type of particles or, however, that the crystallinity is more extended than in the sample obtained with the original method.

TEM images show that nanoparticles have wire shape, as expected, with an average width of 3,4 nm (12%) and long over 300 nm. Some bundles of wires are also visible, likely formed by various shorter wires, a 2-3 nm larger than the single ones. Their length varies from 100 to 300 nm, with an average width of 31 nm (26%). These bundles are also similar to the flower-like nanoparticles made with the ODE method. NW sample also appear stiff and more linear than the one reported in literature[49]. Thanks to the HR-TEM is possible to note that the wires are formed indeed by smaller nanoparticles, melted together with the same crystallographic orientation, [001], that is the same of the nanoribbons[30,32]. To collect good quality pictures of this wires using the HR-TEM to observe the crystalline plane of the single nanowires proved difficult because of the organic capping and their very small width. For the same reason, it was hardly possible to have good statistics for the length of wires into the bundle.

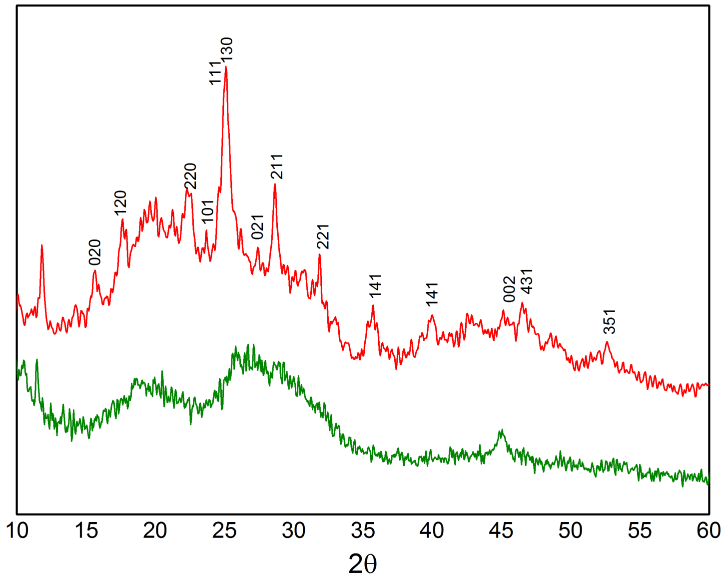

Fig. 2.18: XRD patterns of NW-samples (red) compared with the pattern of a sample obtained using the method proposed by Cademartiri et al. (green)[47,49,65].

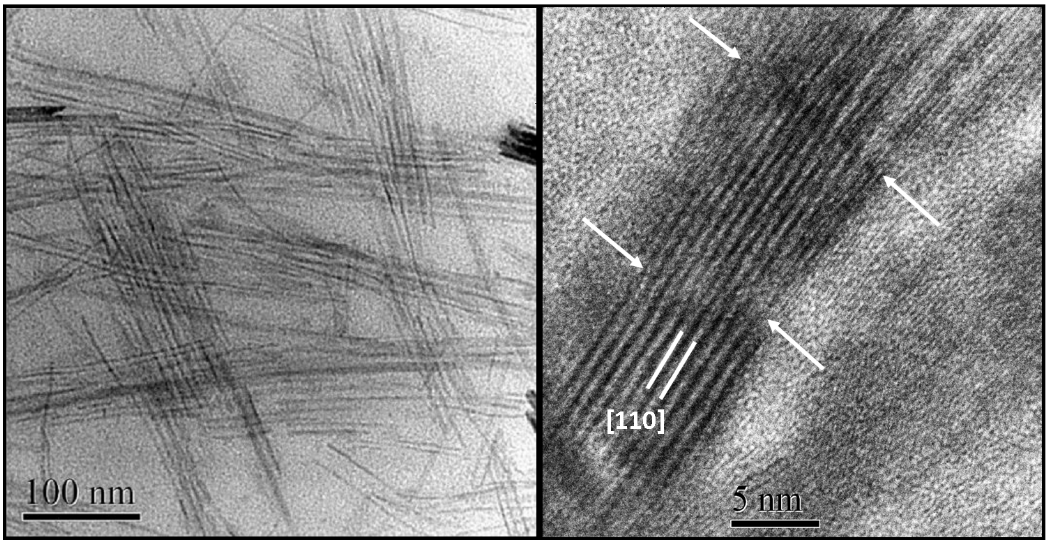

Fig. 2.19: (a) TEM bright field images of NW sample. (b) HR-TEM image of a portion of Bi_2S_3 nanowire, where nanocrystals are iso-oriented along the [001] direction; grain boundaries are present between the nanocrystals (arrows).

2.3 Organic capping on the surface

Usually, samples synthesized by SACS have great stability in organic solvent, due to the organic capping. An organic capping is a shell of surfactants, often a monolayer, that bind with their polar head on the surface of the nanoparticle. It is comparable to a micelle with a solid phase at the center instead of a liquid phase linked to heads of surfactants. The hydrophobic tail makes it possible to disperse a hydrophilic material into organic solvents, producing stable colloids. Moreover, the surfactant guides the growth of the particles during the synthesis, binding with the ion precursors and acting on the kinetic growth, influencing the final morphology and shape. Last, but not the least, the bond between surfactant heads and surface saturate this last one and could prevent some unwanted shallow relaxing effects of the crystal structure. In the following paragraphs, I will show the FT-IR spectra of various Bi_2S_3 samples.

2.3.1 Fourier transform infrared spectroscopy (FT-IR)

Fourier transform infrared spectroscopy (FT-IR) is able to give us information about the organic layer on its surface. Any samples were dried in oven at 40℃ in air and then mixed with KBr and pressed to make a thin pellet. Sometimes, samples dried were too gummy to be used as powder. In these cases, the measurement was carried out putting a drop of the colloidal dispersion on top of a KBr pellet and dried under infrared lamp or oven for minutes. FT-IR spectra were collected by using a Bruker Equinox 55 spectrophotometer in the region from 400 to 4000 cm^{-1}.

Bi_2S_3 - HMS

Fig. 2.20 presents the FT-IR spectra of the HMS sample synthesized with an injection temperature of 170°C and growth time of 6 hrs. Because of the Bi_2S_3 absorption in the infrared range, the spectrum does not have a linear background. In order to not modify the signal position, the background correction was not performed. Signals at 2932 and 2860 cm^{-1} can be attributed at the C-H symmetrical and asymmetrical stretching. These peaks followed by signals at 1460 and 728 cm^{-1}, like in this case, indicate the presence in the sample of aliphatic long chains. Peaks at 1084, 1034, 728 and 698 cm^{-1} can be attributed to an aromatic monosubstituted C-H bending[67–69], while the signal at 3075 and 3037 cm^{-1} are correlated to aromatic or unsaturated chains (containing C=C). The signals at 1498 and 1390 cm^{-1} are due to symmetric and asymmetric stretching of the carboxylate groups (COO^-)[68]. The distance between them, less than 110 cm^{-1}, and the absence of absorption peaks in the range 1725-1700 cm^{-1}[67–69] suggest that a carboxylic acid is present in its dissociated form bonded in a bidentate modes with the bismuth on the surface. Besides, the peak at 1608 cm^{-1} is attributed to C=C groups[70] or to the presence of carboxylate group bonded at the surface with a bridging or unidentate coordination[69]. All signals were expected because the only surfactant used during the synthesis was the oleic acid, a carboxylic acid with a C=C group in its C18 chain, and the organic solvent where the particles are dispersed was the toluene, an aromatic ring monosubstituted with a methyl group.

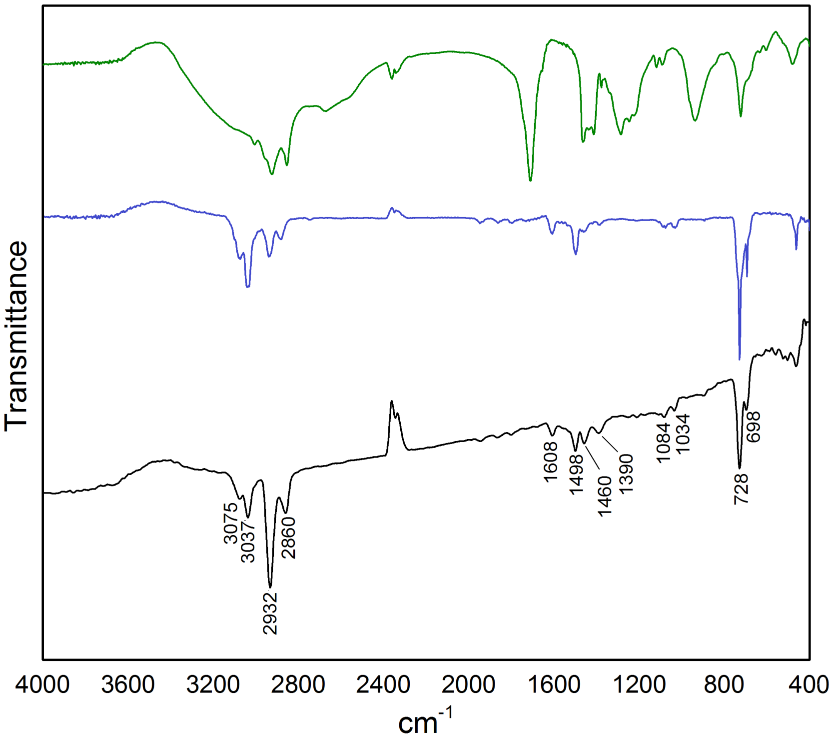

Fig. 2.20: FT-IR spectra of HMS sample (black), toluene (blue) and oleic acid (green).

Bi_2S_3 - OAm

ExS-sample

Mid-infrared spectra of sulfur-in-excess samples confirm the presence of oleic acid on their surface. Long chains characteristic signal are visible in the range 3100-2700 cm^{-1}, 1465 and 720 cm^{-1} [67]. The carboxylic group is indicate by 1549 and 1377 cm^{-1} peaks. The difference between them are attributable to a bridging bond with the nanoparticle surface[69]. The signal at 1710 cm^{-1} belongs to the vibration of reactive carbonyl of carboxylic acid or an unidentate carboxylate[67–69]. The attribution of 1642 cm^{-1} peak is uncertain because it could indicate either the presence of amide groups, a presumable product of the reaction between oleic acid and oleylamine present in the reaction mixture, or that carboxylic acid is conjugated with a double bond or another carboxylic acid[67]. Amides production from these surfactant was recently demonstrated for magnetic nanoparticles via hydrothermal synthesis, covered by similar organic capping[47]. However this sample shows an intensity of the chain signals higher than examples reported in literature[68,71]. Other signals that can prove one of these two alternatives, are not visible. Signals at 990 and 908 cm^{-1} are both attributed to C=C-H out-of-plane bend[67]. Pure vinyl groups were not expected from the reaction but this signal could be due to the C=C in the oleic acid chain. At the same time, we found no proof of the presence of OAm on the nanoparticles surface because no exclusive signals of amine group are present.

ExB-sample

FT-IR spectra show characteristic signals of OA. The sample collected after 30 min of growth has a not linear background due to the Bi_2S_3, as discussed above; it is possible that the particles have lost a portion of their capping during the centrifugation steps, making more apparent the Bi_2S_3 contribution on the final spectrum. The centrifugal force applied on the particles during the centrifugation step pushes them towards the bottom of the flask (often a test-tube) maintaining waste molecules into the solvent; unfortunately, using this method, also a little portion of the organic capping could be entrapped into the solvent. This happens often when the bond between the head of the surfactant and the shallow atoms of the particle is not strong enough to fight against the attraction of the solvent on its tail. No background correction were performed to preserve the spectral position of the peaks.

The two peaks of the carboxylic group in salt form are wider than normal. As visible in Fig. 2.22b, their shape suggests that they could derive from the convolution of individual peaks too close to be resolved. This could be attributed to the presence at the same time of bridging and bidentate carboxylate coordination modes[69]. With the increasing of the reaction time new signals appear in the range 1150-1000 cm^{-1}, that could be due to secondary alcohol stretching or C-O stretching of alkyl-substituted ether[67]. It is therefore possible that OA molecules reacted with each other to form an ether. No specific signals of OAm are visible.

StS-sample

Signals are all attributable to the presence of OA. The signal around 1540 cm^{-1}, usually paired with another narrow signal at 1420-1300 cm^{-1} and indicative the presence of COO$^-$ groups, is absent[67]. However, the signal at 1463 cm^{-1} appears wider than usual. It is so possible that the peaks of the doublet due to the carboxylate group are so close together to overlap with the 1460 cm^{-1} signal, characteristic of long organic chain, making it wider. The peak at 1716 cm^{-1} is instead attributable to not dissociated carboxylic acid or unidentate carboxylate while the peak at 1631 cm^{-1} could be due to carboxylic groups conjugated between them or to amide functional group[67]. These observation are in agreement with the poor colloidal stability of the sample because its surface could be covered by only a little fraction of molecules in bidentate mode[69] and mostly covered by not dissociated (and eventually not bonded on the surface) oleic acid molecules; these last ones can destabilize the colloidal solution and to be easily removed by centrifugation.

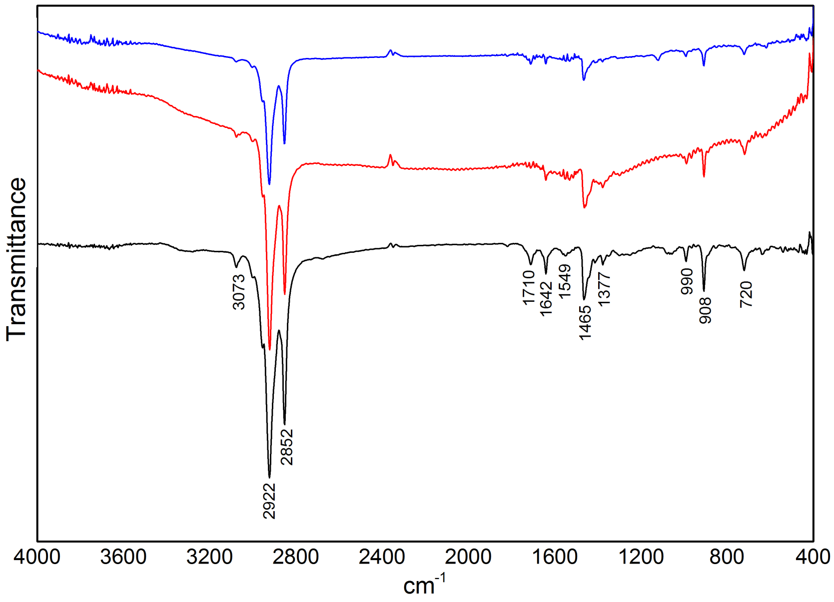

Fig. 2.21: FT-IR spectra of ExS-OAm sample at different reaction time and temperature, 120°C and 10 min of growth (blue), 170°C 10 min (red) and 30 min (black) of growth.

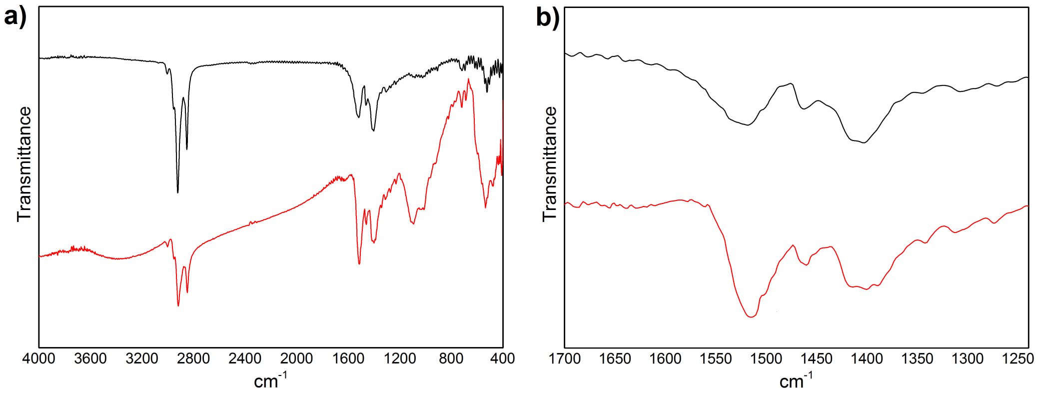

Fig. 2.22: (a) FT-IR spectra of ExB-OAm sample after 10 min (black) and 30 min (red) of growth. (b) Detail of 1700-1300 cm^{-1} range.

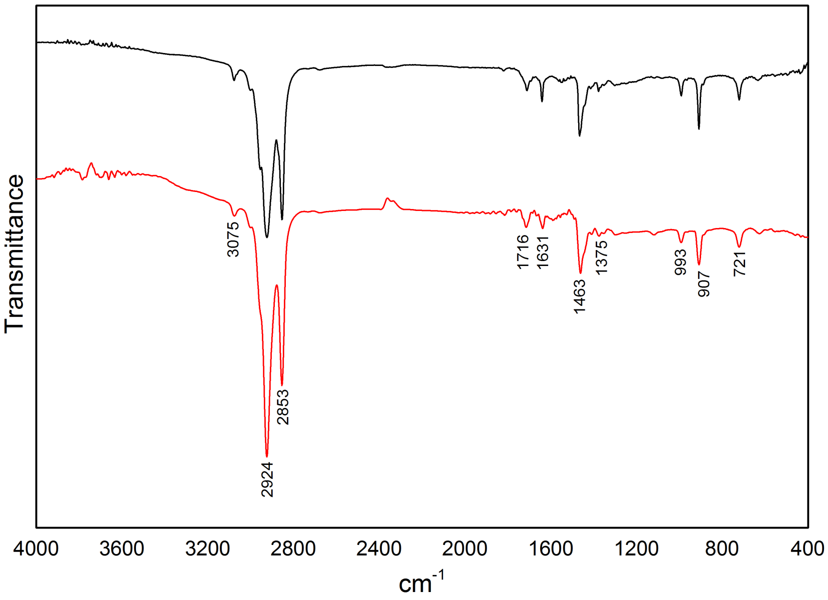

Fig. 2.23: FT-IR spectra of StS-OAm sample after 10 min (black) and 30 min (red) of growth.

Bi_2S_3 - NW

This synthesis was performed without the presence of oleic acid, so the only surfactant that could act as a capping agent was the oleylamine. For this reason, and because FT-IR signals of the amine are similar but lower in intensity and broader than the hydroxyl or carboxylic group[67], in Fig. 2.24 are shown the spectra of the nanowires compared with the pure oleylamine one. In addition to the signals of long organic chain (OA and OAm are different only by the functional group), few new peaks are visible. The 1614 cm^{-1} peak could be due to the N-H bending of the primary amine functional group[67,72], to the NH^{3+} stretching[71] or also the stretching of C=C group in the chain[73]. The hypothesis of NH^{3+} presence is supported by the vanishing of signals at 3370 and 3288 cm^{-1}, characteristic of NH_2 stretching, visible in the OAm pure spectra. A broad weak band around 1520 cm^{-1} and the lowering of 1377 cm^{-1} peaks could also indicate the transformation of pure primary amine groups in something else. The difference between the two spectra in the range 900-700 cm^{-1} suggests that the C=C group might have reacted. The signal at 672 cm^{-1}, attributed at C-S stretching, and 618 cm^{-1}, the S-S disulfide stretching[67], suggests that the chains on the surface are not due to pure oleylamine but to an oleylamine derivate. The sulfur precursor was an OAm/elemental sulfur solution. Thomson et al.[74] propose different reaction mechanism between S and OAm that would allow the presence of NH^{3+} and/or $R\text{-}C(S)NH_2$ groups. Furthermore, S is able to form copolymers with oleylamine reacting with its carbon-carbon double bond[75]. These pieces of information do not give us a certain proof about the type of functional group bonded on the nanowires surface but are in agreement with our observations.

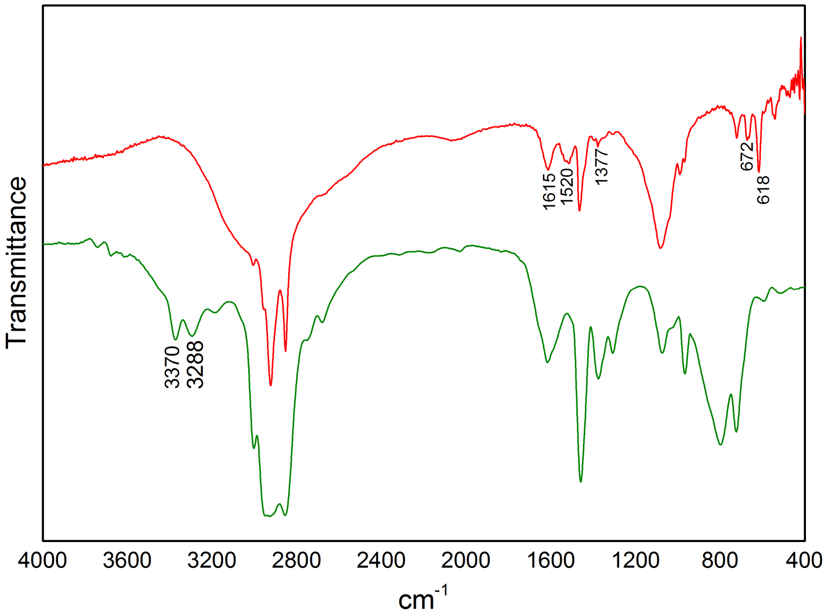

Fig. 2.24: FT-IR spectra of NW sample (red) compared with the OAm (green) spectra.

2.4 Optical properties

UV-Vis spectra were collected by using a Varian Cary 50 UV-Visible spectrophotometer equipped with a fiber optic dip probe (1 cm optical path length), Xenon lamp and Czerny-Turner monochromator, with a range of 190-1100 nm. All samples were analyzed in colloidal form putting them inside a cuvette, crossed then by the light.

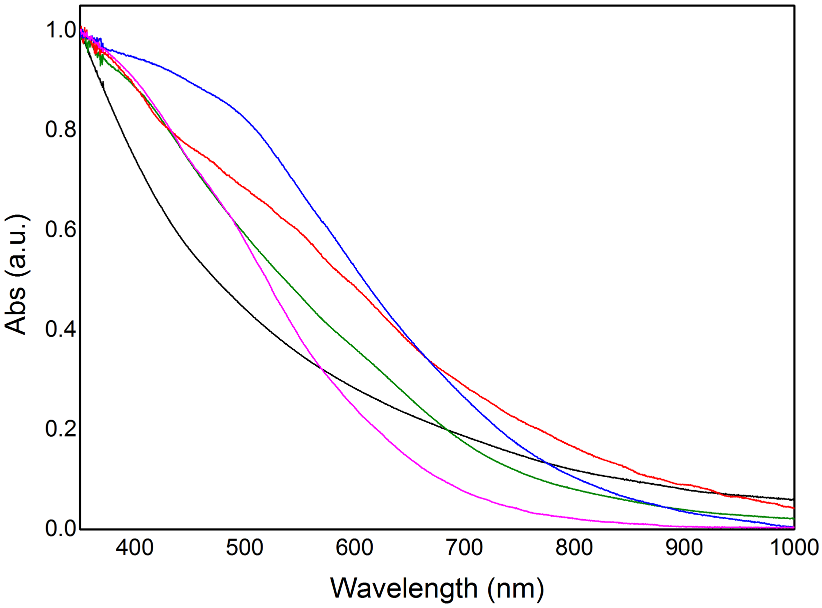

Fig. 2.25: UV-Vis absorption spectra of HMS (black), OAm-ExB (red), OAm-ExS (blue) OAm-StS (magenta) and NW (green) samples.

The colloidal stability was sometimes too low to allow us to collect a good UV-Vis absorption spectrum for all samples. However, their mainly show a curve that go to zero at around 900-1000 nm according to the literature[43,50]. In Fig. 2.25 are reported all spectra of Bi_2S_3 samples; for sake of comparison, are shown only sample synthesized at 170°C for 30 min. HMS and NW spectra are the most similar to the ones reported in literature[43,50]. OAm-samples show a different slope below about 500 nm. All these differences are due to defect of the materials.

None of our Bi_2S_3 samples have shown photoluminescence (PL) emission. In literature are not reported PL spectra of Bi_2S_3 nanoparticles except for nanowires with diameters higher than 50 nm up to 300 nm, produced with different synthesis method that does not use capping agents[41,76,77], or in combination with other metals like iron[78] or silver[79]. So, this is in agreement with our observations.

2.5 Conclusions

From all these results, it is possible to formulate some conclusions.

SACS synthesis is an useful and relatively easy method to produce chalcogenides in colloidal form. Acting on temperature and/or time of reaction it is possible to have a control on nanoparticles dimensions and shapes. Temperatures too low produce small nanoparticles with a large size distribution. Increasing the temperature, nanoparticles assume a common morphology with a narrower size distribution. At the same time, also the crystallinity improves and so we might expect lower concentration of shallow defects; this is an important consideration when a material is thought for optical applications.

The growth of the nanoparticles is driven by surfactant agents. The presence of only oleic acid (OA) produces spherical/rods nanoparticles with also a good colloidal stability in organic solvent. A gradual addition of oleylamine (OAm) promotes the growth of the particle along the [001] crystallographic direction, the same of its nanoribbons, increasing elongation of the nanorods until to obtain ultrathin nanowires, when only OAm is present. This is in agreement with the preliminary XRD observations because the larger peaks are correlated to smaller particles; also changes in shape explains the differences of intensity peaks. In any case, XRD characterizations prove that methods used produce always bismuth sulfide in orthorhombic crystallographic phase.

TEM confirms the crystallinity of the particles and also their nanodimensions, ranging from 3-4 to hundreds nanometers, with large variety of shapes from spherical to wire and also macro structures like the flower-like one of the ODE sample. It is interesting to investigate the different speed of growth as a function of the employed surfactant. HMS method produces little spherical nanoparticles that turn into rods within hours. The OAm method, instead, produces instantly nanorods with width similar to the first method but with larger lengths achieved within minutes. This means that this method is faster than the HMS one but, for the same reason, it is more difficult the control of shape and crystalline quality of the final product. The lower stability in organic solvent is another point against this method. NW particles grow fast too, but with a different mechanism. While the growth of the other particles appears due to Oswald ripening, nanowires were formed by small nanoparticles welded together with the same orientation, that is the same of the nanoribbons. As proposed in literature[47] the mobility of the charge carrier is higher perpendicular to nanoribbons plane, so the elongated shape of the nanoparticles could be very useful to increase its electrical properties and the final efficiency of the optical devices in which they will be used.

Unfortunately, only HMS nanoparticles were colloidally stable enough to be used in the solar cells fabrication, as shown in Chapter 3. HMS and NW samples are stable for years while the OAm-samples are stable for days or weeks, except when performed in excess of sulfur, which colloid could be stable for months, at equal washing steps carried out. Centrifugation step numbers could damage this stability. HMS and NW sample are not damaged also after several treatments but the NW also needs to be very diluted or tend to form a deposition on the flask bottom. OAm-samples instead see their stability very compromised after only one or two washing steps. Of course, if the particles are not cleaned enough from the excess of surfactant, the sample remains dirty, gummy and insulating when dried and difficult to characterize. In fact, mostly for the ExB and StS-sample, we see the [002] peak in the XRD patterns very intense and narrow but also its disappearance if we wash the sample more times. So, this signal could be due to an organic phase in excess or to a preferential orientation due to the higher concentration of organic capping molecules. Finding an answer to this question is difficult because obtaining a clear TEM image is impossible if the organic excess is not removed; the organic layer interferes with the electron beam giving hazy pictures, without a good resolution. At the same time, FT-IR shows us several signal more that are not linked with the real capping of the nanoparticles. For all these reason, TEM and FT-IR data come all from clean samples, making sometimes visible the presence of aggregates of nanoparticles or higher contribution in the spectra of the Bi_2S_3.

If the HMS sample does not suffer the negative effect of the cleaning steps, it could also lose its stability already from the synthesis. The reproducibility of this method, in fact, is not perfect because sometimes it fails, producing good nanoparticles but completely unstable. This could be due to the HMS, a compound that quickly reacts with oxides or water to produce the corresponding silane or H_2S. This one is a toxic smelly gas often used for the synthesis of several sulfides including Bi_2S_3 [62,80]. We cannot exclude that this gas does not have a role during our synthesis but, if present, it is confined into the reaction flask. The HMS could be polluted by a reaction with the humidity of air, during the injection step or be polluted already before to use. Currently our ratio of success with this method is around 80%, considering as success a colloidally stable sample because pure and crystalline nanoparticles have been always obtained.

FT-IR characterizations has shown that the principal capping agent on the nanoparticles surface was the oleic acid, when present. This one was seen in all samples analyzed (except of course the NW), while the oleylamine was not present or at least visible. In fact, we cannot exclude completely the OAm presence on the surface of the particles because its signals are very similar to the carboxylate ones. Also, some peaks could be attributed both to olefinic molecules or to amide presence. In the second case, the reaction between oleic acid and oleylamine could produce two long chain molecules that could bond with the surface, probably through the amine group[47], or suffers the steric hindrance. It is also possible that the organic chains interact between them, doing a multilayer capping. This one could influence the colloidal stability, in function of the orientation of the external molecule functional group, and be easily removed with the centrifugation. All OAm-samples show moreover a low intensity of the COO^- salt signals, the pair at around 1500 and 1300 cm^{-1}, with respect of the C-H stretching and chain signals. This difference could depend to a strong chemical bond between the oxygen of the carboxylate group and the surface. These bonds, obviously stronger than a physic bond, reduce the freedom of movement of the atoms, and so the expected vibrations of the functional group. On the other hand, poor stability of the sample and the progressive loss of stability, suggests that only a very little amount of surfactant molecules are bonded strongly on the surface while the others could be easily removed. Washing steps affect also the quality of the FT-IR spectra, increasing the contribution of the Bi_2S_3 on its. In fact, more a sample is "washed" higher is the distortion of the spectra suggesting that the particles are less covered by organic materials. Similar effects are visible in the HMS-sample spectra but for this one the intensity of the carboxylate signals is always higher than OAm-sample ones.

The similarity of the UV-Vis spectra of the samples suggest that the energy bandgap (E_g) could be, in according with the literature, between 1,3-1,8 eV[34–42]. The total absence of photoluminescence could be due to the presence of traps that nullify this phenomenon. This is not a big problem because for a photovoltaic application is most interesting the production of the charge carrier and so it is most important that charges could pass through the various device materials. The absence of photoluminescence is in agreement with the literature which connect this to the tendency of the Bi_2S_3 to suffer of sulfur vacancies. No Bi_2S_3 nanoparticles PL emission has been observed until the writing of this thesis except for mixed sulfide based on bismuth and other metals[78,79].

Chapter 3

Bi_2S_3-based solar cell prototypes

A solar cell (or photovoltaic cell) is a device which converts solar energy into electric energy. It is formed by light absorbing materials connected to an external circuit. The absorption of photons produces excitons that are then split into two charge carriers, forming a photocurrent with their motion to electrodes. When the cell is in dark, it can be considered as a diode; however, under illumination, a photocurrent is produced which opposes to the dark current and so the Shockley equation for an ideal diode (Eq.(3.1)) must be adapted adding the contribution of the current density generated, J_{sc} (Eq.(3.2), Fig. 3.1).

$$J_{dark} = J_o(e^{\frac{qV}{kT}} - 1) \tag{3.1}$$

$$J_{light} = -J_{sc} + J_o(e^{\frac{qV}{kT}} - 1) \tag{3.2}$$

V is the voltage applied to the electrodes, q is the electron charge, k the Boltzmann constant, T the temperature of the p-n junction and J_o is the saturation current which depends on the characteristics of the p-n junction, as shown in Eq.(3.3).

$$J_o = q\left(\frac{D_p n_i^2}{L_p N_D} + \frac{D_n n_i^2}{L_n N_A}\right) \tag{3.3}$$

D_p and D_n are the diffusion coefficients of electrons and holes while L_p and L_n are their diffusion lengths, n_i is the intrinsic density of carriers and N_D and N_A are respectively the donor and acceptor concentrations[81].

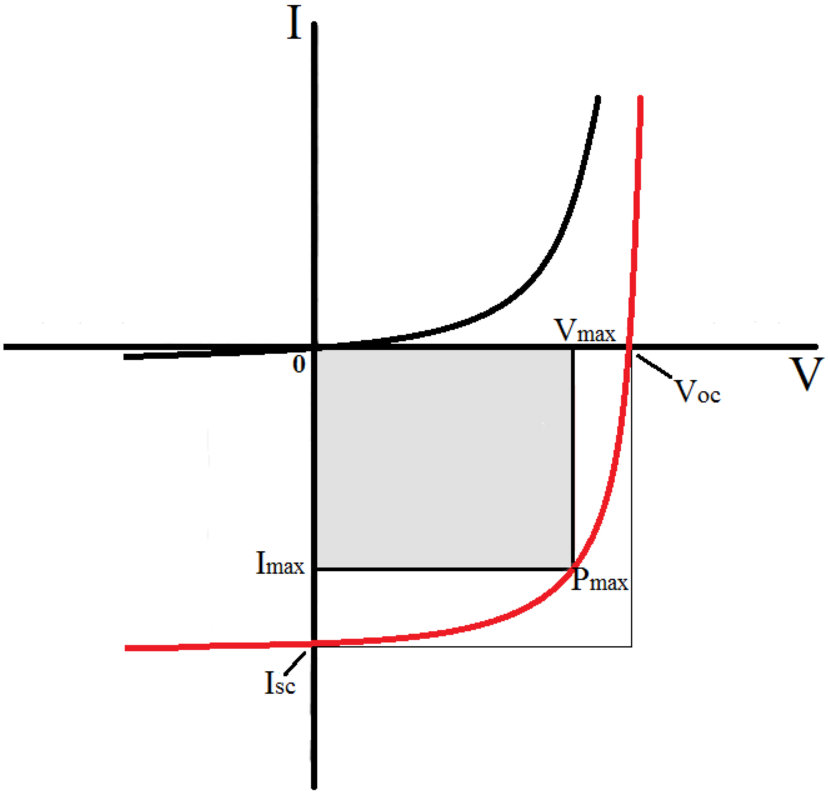

Fig. 3.1: I-V curve of solar cell in dark (black) and under illumination (red)[81].

The intensity of the generated current is correlated to the intensity and energy spectrum of incident light. Quantum efficiency is a parameter which quantifies the probability that an incident photon produces an electron; it can be defined as a function of the photon energy. It is given by the ratio between number of carriers collected by the cell and number of incident photon of a given energy. Similarly, the efficiency of the solar cells (η) is given by the ratio between the power generated by the cell and the power of incident light, expressed in percentage. The maximum power produced by the cell could be graphically measured or calculated using some parameters that can be extracted from the I-V characteristics. Such parameters are the short circuit current density, J_{sc}, the open circuit voltage, V_{oc}, and the fill factor, FF[81].

- Short circuit current density, J_{sc}: It is the current per unit area which passes through the cell when the voltage applied to the electrodes is zero (see Eq.(3.2)); it is also the maximum density of current obtainable from the cell. This parameter depends on the incident light, its intensity and spectrum. For this reason, most of the cell measurements are performed with a spectrum standardized to the AM1.5 spectrum, with an intensity of 1 kW/m^2 (one sun).[81]

- Open circuit voltage, V_{oc}: It is the maximum voltage available from a solar cell. It is the voltage value at current zero and it is equivalent to the condition when the dark current and short circuit photocurrent exactly cancel out (see Eq.(3.2)). Eq.(3.4) is the V_{oc} equation for an ideal diode and it shows that the V_{oc} is linked to the saturation current, which is function of the diffusion length of the charge carriers. It is possible to consider the V_{oc} indicative of the amount of charge recombination into the device. V_{oc} is also directly correlated to the bandgap of the cell. In general, V_{oc} is always lower than E_g/e by around 0,3 to 0,5 eV[81,82].

$$V_{oc} = \frac{kT}{q} ln\left(\frac{J_{sc}}{J_o} + 1\right) \tag{3.4}$$

- Fill Factor, FF: It is the ratio between the maximum power from the cell, calculated by the product of J_{max} and V_{max}, and the product of J_{sc} and V_{oc} (Eq.(3.5),(3.6)). So, graphically, it is a measurement of the squareness of the J-V curve (Fig. 3.1). Usually it is expressed in percentage; the higher this value, the more similar the cell to the ideal one[81].

$$FF = \frac{J_{max} \cdot V_{max}}{J_{sc} \cdot V_{oc}} \tag{3.5}$$

$$\eta = \frac{P_{max}}{P_{in}} = \frac{J_{max} \cdot V_{max}}{P_{in}} = \frac{J_{sc} \cdot V_{oc} \cdot FF}{P_{in}} \tag{3.6}$$

Electrically, the solar cell is equivalent to a current generator in parallel with a diode (Fig. 3.2). An ideal cell produces a photocurrent proportional to the light intensity but in a real cell the photocurrent is also influenced by the resistances of the device. These resistances are so correlated to the quality of solar cells and they are classifiable in two main categories: shunt and series resistances.

- Shunt resistance (R_{sh}) can be attributable to a resistance in parallel to the cell. It derives mostly from manufacturing defects and impurities. For the proper functioning of the cell, this resistance must be as large as possible to allow the motion of the electrons toward the electrode passing through all the layers of the cell. So, this resistance is important to promote the electron flux through the cell rather than in a single layer. In fact, low value of this resistance affects the FF causing also a decreasing of the V_{oc} value.

- Series resistances (R_s), instead, must be as low as possible, because they are linked to the quality of the interfaces between layers and with the electrodes. High values of this resistance affect the FF and the J_{sc}.

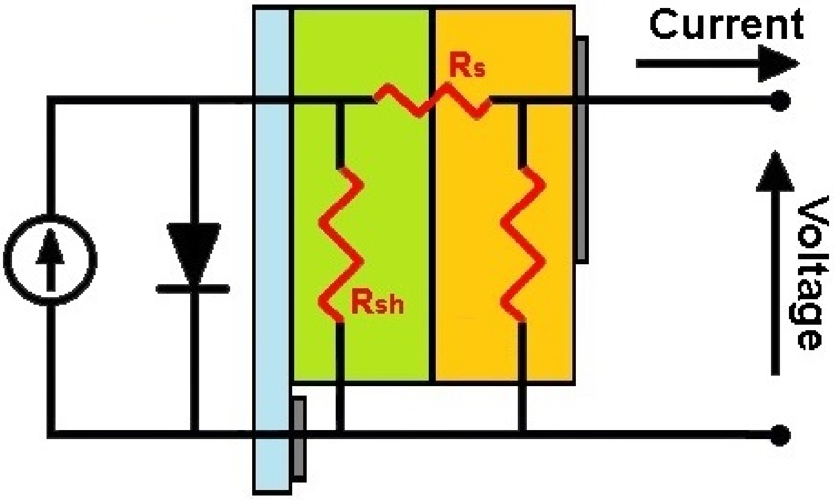

Fig. 3.2: Equivalent circuit of a solar cell compared with a simple scheme of a solar cell. Green and orange bands represent the semiconductor which form the “active layer” of the device.

Bismuth sulfide shown in the previous chapter is a potentially useful semiconductor for this application. The choice to synthesize it directly in colloidal form was born from the idea to tune its size, in such a way to have a control on bandgap energy (as explained in Chapter 1), and to produce homogeneous films on conductive support using appropriate deposition methods, building a ‶solution processed solar cell″, SPSC. These cells are based principally on colloidal nanoparticles, used to produce layers in a sandwich-like structure. One or more semiconductor layers can work as the active layer of the cell, absorbing light in a certain range of wavelengths as a function of the materials energy gap.

3.1 Device architectures

In a solar cell, after the photon absorption, excitons are produced. These excitons are electron-hole couples which interact through Coulomb forces. The efficiency of a solar cell is linked to the number of excitons generated which split into charge carriers at the interface between acceptor and donor materials. Each exciton has to move from the region where it was generated to the interface faster than their recombination process. Exciton diffusion length, the average distance which it can move until it recombines, depends to the material; for example, it is about 5-10 nm in organic solar cells. Moreover, also the charge carries must be able to reach the electrodes before recombining. The characteristics of the device must be chosen carefully, taking into account too the different carrier mobilities into various materials (less than 0,1 $cm^2/V{\cdot}s$ in molecular materials with respect of 100-10000 $cm^2/V{\cdot}s$ in crystalline inorganic semiconductors) and that electrons could have higher mobility than holes[81].

During my work, two different cell architectures were tested: the "bilayer" and the "bulk heterojunction" solar cell. Both of them were built layer by layer with annealing steps when required. The electrode on top of the cell was a metallic contact (Al, Au, often Ag) deposited by thermal evaporation while the other contact was a transparent conductive glass. Indium Tin Oxide, ITO, and Fluorine doped Tin Oxide, FTO, glasses were chosen for this application and used as first substrate where to build all the other layers.

3.1.1 Bilayer solar cell

The bilayer solar cell (Fig. 3.3-left panel) is formed by two layers of different semiconductors in contact with each other. One of them is the n-type semiconductor, which supplies free electrons (electron donor), and the other one is the p-type semiconductor which supplies free holes (electron acceptor).

This is the traditional architecture of silicon-based solar cells. The interface of the semiconductor is considered the true active layer of the cell because the split of the carriers occurs on it. After the splitting, electron and holes will move to the respective electrodes. The thickness of the semiconductor layers must allow the excitons to move efficiently toward the interface before they recombine. If the layer is too thick, the efficiency of the cell will decrease because of a good amounts of excitons recombine before to reach the interface. At the same time, a layer too thin will not absorb enough solar photons and so the number of excitons generated will be poor. An ideal thickness should be similar to the exciton diffusion length, allowing also a good solar light absorption. Another feature of this architecture is that it is planar and so, to produce enough energy, it could be necessary to have available a large interface area, which also needs to be illuminated homogeneously. Obviously the higher is the area, the higher will be the possibility to have portions of the cell not illuminated because of shadows, for example, and so to have a power loss.

3.1.2 Bulk heterojunction (BHJ) solar cell

The active layer of this cell is made by two materials blended together (Fig. 3.1-right panel). Like in the bilayer, the materials are donor and acceptor semiconductors and the charge carriers are split at the interface. This architecture, however, should be more efficient than the bilayer one because the blend increases the interface area. For this reason, the blend layer is considered such as an unique active layer. An ideal active layer for this cell should have the donor and acceptor semiconductor arranged in order to maximize their interface but also to give an advantageous route to the carriers to reach the electrodes. Unfortunately, the blend is often a random mixture of two semiconductors, one of them organic into the hybrid solar cell, and so obstacles for the carriers motion could be present. Moreover, it must be considered how much deeply a photon can penetrate into the blend. With an active layer too thick, in fact, the core of the layer could not be illuminated and so the number of excitons generated could be poor. At the same time, it is important to combine two materials which, with their absorption coefficients, can be able to absorb the solar spectrum as much possible. The final thickness of the blend layer should therefore be comparable to the penetration depth of the light, the exciton diffusion length and the charge carriers mobility.

Usually, BHJ have the active layer in contact with other materials with the aim to promote the carriers separation thus increasing the produced photocurrent. These are the electron transport layer (ETL) and the hole transport layer (HTL)[83,84]. The ETL, through its energy levels, promotes the motion of the electron to the metallic contact, blocking instead the holes. Most used ETL are large bandgap semiconductor such as TiO_x or ZnO that are also transparent to visible light[24,84–90]. The same roles, but blocking the electrons, is played by the HTL. This material is often constituted by high molecular weight polymers, like P3HT or Spiro-OMeTAD or metal oxides, like MoO_3, V_2O_5, WO_3, NiO[84]. Several ETL/HTL materials are commercially available but sometimes it is necessary to synthesize them[83,84].

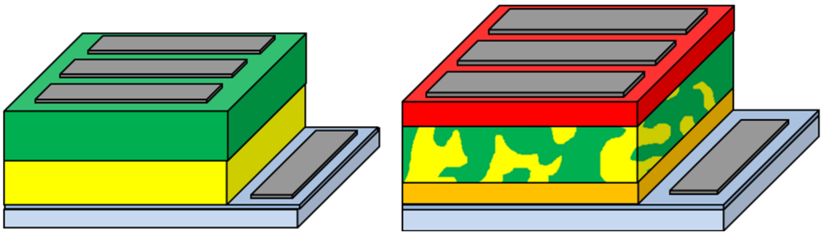

Fig. 3.3: Schemes of (left) bilayer and (right) bulk heterojunction solar cells. Green and yellow colors represent donor and acceptor materials, separated in the bilayer and blended together in the bulk heterojunction solar cell.

For both these architectures, it is important that energy levels are favorable for the faster exciton dissociation, the subsequent charge separation and the motion through the phases without charge recombination[84].

3.2 Building the layers

All the layers of a solar cell need different treatments as a function of the nature of the used material. Nanoparticles, for example, must be deposited onto the substrate in a homogeneous thickness, without holes in the layer. Deposition techniques like dip or spin coating could be ideal for this aim. Other materials, like basic oxides could be synthesized and grown directly on the substrate. So, techniques like sol-gel synthesis, chemical bath deposition or chemical vapor deposition are commonly used[88,91–93]. In this section, techniques used for manufacturing of Bi_2S_3-based solar cell prototypes will be shown.

Sol-gel synthesis was used to produce TiO_2 and ZnO layers. All the other materials were made using dip coating or, more often, spin coating deposition methods. Metallic contacts were deposited by thermal evaporation.

3.2.1 Deposition methods

Dip coating

In this procedure, a substrate is dipped vertically into a solution or a colloidal dispersion for seconds and then let dry in air for several minutes. The withdrawal speed and concentration of colloids can modify the thickness of the final film. Viscosity, surface tension and drying rate of the bath solution play an important role in the final film quality. All steps can be performed automatically, setting a motor controlled arm holding sample on a pre-determined motion path. At the same time, dipping the substrate into a single bath could contaminate the colloidal solution used in particular if several steps are needed, such as in our case. Nanoparticles produced by SACS method are characterized by an organic layer on their surface which is often an electrical insulating and so several coating steps could be necessary to exchange this layer with another. First, the substrate is dipped into the colloidal solution of nanoparticles. Then, the sample will be dipped into a solution of a different capping agent which will replace the original one and, finally, the sample will be dipped into one or more solvents to clean it from the impurities. All these steps are repeated usually three to five times.

Spin coating

One or more drops of a solution or a colloidal dispersion are dropped onto a horizontal substrate. Then, the substrate is accelerated up to the desired rotation speed, usually around 3000 rpm (rounds per minutes). During the spinning, the solution covers homogenously the surface and the solvent evaporates. Rotation speed, temperature, concentration and affinity between liquid and substrate can influence the thickness of the final film but also viscosity, surface tension and drying rate of the solvent are important factors. Cast of the liquid can be done before or during spinning, respectively called “static” and “dynamic” methods. With this method, the risk of pollution of the colloidal solution used is reduced, but a fair amount of it is wasted while spinning out of the substrate.

3.2.2 Sol-gel methods

The sol-gel method is based on two steps. First, it is necessary to prepare a 〝Sol〞, a colloidal solution of precursors. Then, the solution is dried to form a 〝Gel〞, a network of particles or polymers that after annealing could produce homogeneous films of oxides. Usually, this synthesis is used to produce metal oxides and it is a method often used for silicon or titanium oxides[87–89]. Often the metal precursors are alkoxides or carboxylate salts. When the solvent is not water, a stabilizer is added, like amine. The annealing temperatures are different as a function of the materials and the type of crystal that we want to obtain[88–90]. The materials synthesized with this method are titania (titanium oxide, TiO_2), zincite (zinc oxide, ZnO) and aluminium doped zinc oxide (AZO).

Titania - TiO_2

A solution of titanium diisopropoxide bis(acetylacetonate) (75 wt%, Aldrich) 0,15 M in isopropanol was spinned on the conductive substrate at 3000 rpm for 30 sec, followed by two spinning steps at the same condition with a 0,3 M solution. The substrate was then dried at 125°C for 10 min and heated at 550°C for 15 min in air[94].

When in addition to this compact layer (cp-TiO_2) was necessary a mesoporous titania layer (mp-TiO_2) too, commercial titania paste (Aldrich-Dyesol, 19 wt%) was spin-coated at 3000 rpm for 30 sec and then heated at 500°C for 30 min.

With or without the mesoporous layer, a final treatment with $TiCl_4$ was performed to activate the titania surface. 300 μl of $TiCl_4$ 2M in H_2O was added to 40 ml of water. The substrate covered by titania was dipped in this solution for 30 min at 70°C in a covered Petri dish. After a washing step with distilled water, the film was dried in air and heated again at 500°C for 30 min.

Zincite - ZnO

A solution of 0,5 g Zn acetate dihydrate, 5 ml of methoxyethanol and 0,142 ml of ethanolamine was prepared at room temperature by stirring. Then 6-8 drops was spin-coated at 3000 rpm on a substrate and heated at 200°C 30 min in air to obtain a transparent layer of ZnO[24].

Aluminium doped zinc oxide - AZO

2,2 g of Zinc acetate dihydrate and 0,016 g of aluminium hydroxide acetate were dissolved in 100 ml of ethanol at room temperature. To stabilize the Al-Zn complex, 0,61 ml of monoethanolamine was added to the solution. Then, it was refluxed for 3 hrs at 80℃ under stirring to get a transparent solution. Spin coating (3000 rpm) was used to coat the substrates that were heated at 260℃ 10 min in air to obtain the transparent AZO layer[85].

3.2.3 Preliminary tests

The filmability of all the materials was tested first on soda lime glass and then on conductive glass. In this way, it was possible to estimate quality of every film using different spinning/dipping speeds, volumes and concentration of solution needed and coverage rate of the surface. Dip and spin coating have demonstrated to be suitable to produce films with a controlled thickness acting on immersion and withdrawal speed, for the first one, or spinning speed, for the second one.

Concerning the bismuth sulfide layer, conductivity measurements were performed to observe the presence of photoconductivity and so demonstrate that this material can be used as active layer in a cell. By dip coating, few layers of bismuth sulfide were deposited on a soda-lime glass. The glass was dipped into the colloidal solution for 60 sec, with an immersion/withdrawal speed of 500 mm/min, to form the layer of nanoparticle. This procedure was repeated not less than 5 times to obtain a thick enough film. Then, by sputtering, circular gold contacts were deposited with 1 mm distance between them. HMS-sample produced the better film, taking into account the homogeneity and surface coverage, while the OAm-samples did not cover well enough the glass in the same conditions. For such reason, more deposition steps were needed to reach an acceptable coverage of the substrate surface but unfortunately without a homogeneous thickness. NW-samples, instead, did not produce a film due to low concentration, unfortunately necessary to maintain its colloidal stability.

It is important to note that the organic capping of this colloidal nanoparticles is made by long chain molecules. These are useful to cover and stabilize the particles into apolar solvents and also help the formation of the film when dried but are also electrical insulators. For such reason, a measurement of the current as a function of applied voltage was carried out both before and after ligand exchange treatments with ethanedithiol, EDT. The treatment consisted in immersion, by dip coating, of the bismuth sulfide layer in an EDT 2 vol%. in acetonitrile (ACN) solution for 120 sec, followed by dipping in ACN for 30 sec; this treatment was repeated for each layer of sulfide, always with an immersion/withdrawal speed of 500 mm/min.

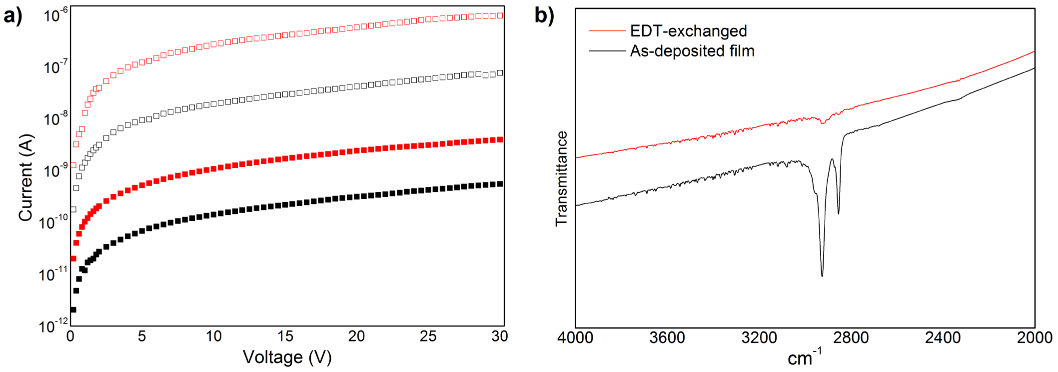

Fig. 3.4: (a) I-V measurements performed in dark (black) and under illumination (red). Full squares indicate the sample with its original organic capping; empty squares indicate the sample after ligand exchange treatment. Current values are reported in logarithmic scale. (b) FT-IR spectra detail of HMS sample before (black) and after (red) ligand exchange treatment.

For the I-V measurement, a halogen lamp was used positioned vertically over the sample. The measurements show an increase of an order of magnitude in the conductivity under illumination with respect to the dark. This is due to the photocurrent generated from the electrons excited to the conduction band with the photon absorption, demonstrating that the Bi_2S_3 photoconducts and could be used as active layer in suitable devices. Further increase of the measured current, up to two order of magnitudes, is visible after the ligand exchange treatment both in dark and under illumination, proving the insulating properties of the capping and the advantages of removing it (Fig. 3.4a). The quantitative efficiency of the ligand exchange is visible from the FT-IR spectra of the Bi_2S_3 film collected before and after the treatment. The characteristic signal of a long organic chain (shown in Chapter 2), between 3000 and 2800 cm^{-1}, almost disappears after the substitution of the oleic acid, a C18 organic molecule, with the shorter EDT, an only C2 chain (Fig. 3.4b). Similar ligand exchange treatment has been performed directly on the colloidal nanoparticles solution, adding the exchange agent in excess of the original capping molecules and stirring for a time varying between few minutes and 24 hrs. The result was an effective replacement of the insulating long chain capping with the short chain one. The capping agent tested were EDT, tetrabutylammonium iodide (TBAI) and dimercaptosuccinic acid (DMSA). Unfortunately this process produced also a strong aggregation of the nanoparticles and caused the loss of their colloidal stability both on organic and polar solvents. Due to this observation, all the ligand exchange treatments performed in the later stages have been made directly on nanoparticle films.

The effect of thermal treatments on the conductivity of the film has been also studied. Performed under inert atmosphere, to avoid the oxidation of the material, these measurements show that annealing treatments could increase the conductivity of the bismuth sulfide film, both in dark and under illumination. Unfortunately, over about 260°C the conductivity is compromised by a permanent degradation of the film which loses its conduction properties, as visible in Fig. 3.5, probably due to the thermal decomposition of the material.

Same measurements, under similar conditions, were performed on the OAm-

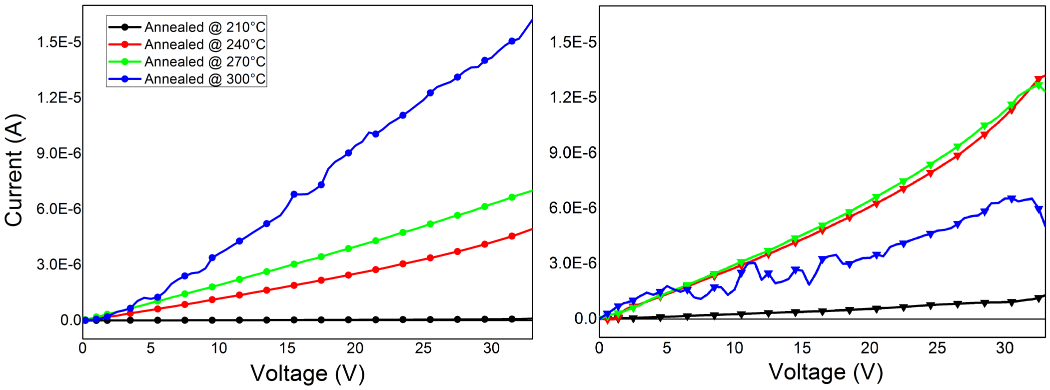

Fig. 3.5: I-V measurements of HMS-sample film after annealing treatment (a) in dark and (b) light.

samples, in particular on the ExS ones. Similar results were obtained. The ligand exchange treatment with EDT increases the conductivity of the film both in dark and under illumination. Unfortunately, even after the improvement, conductivity is still low compared to the HMS-sample results. In particular, the ligand exchange produces an improvement of the electric properties only if the film is not thermally treated. Over 150°C the best I-V curve was collected for the film no ligand exchanged. Also the direct increase of the detecting current with the temperature is visible only for the non-exchanged film and for treatment temperatures below 260°C. If samples were treated with EDT before the thermal treatment, the I-V measurements were not reproducible. This could stem from inhomogeneities of the film due to the nanoparticle nature. Their capping, shape and the manner in which they aggregate on the substrate surface could produce several defects on the film thus affecting the charge transport.

Poor filmability of NW sample and the low conductivity showed by OAm samples, caused us to choose the HMS-sample as a standard to the manufacturing of all the following cell prototypes.

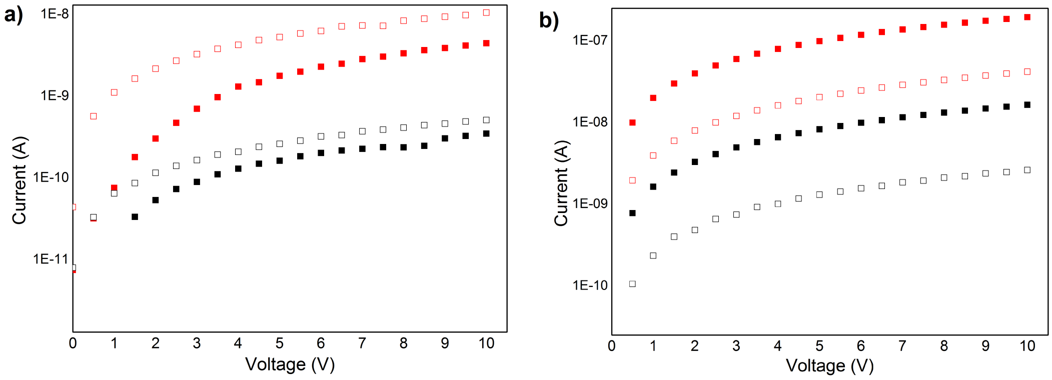

Fig. 3.6: I-V measurements of the ExS-OAm film on soda-lime glass, performed in dark (black) and under illumination (red) with (a) the film maintained at room temperature and (b) after thermal treatment at 240°C before to deposit the Au contacts. Full squares indicate the sample with its original organic capping; empty squares indicate the sample after ligand exchange treatment. Current values are reported in logarithmic scale.

3.2.4 Solar cell

The construction of any single prototype requires some primary steps, resumed in Fig. 3.7. The conductive support used as electrode (ITO or FTO) was subjected to etching treatment, to remove a portion of the conductive layer (Fig. 3.7a and Fig. 3.7b). About the 60% of the area of the glass was covered with adhesive tape after being washed under distilled water and ethanol flow and being dried with clean dry air. Then the glass was put into a becher with 50 ml of distilled water and zinc powder. 20 ml of HCl 37% was added and let react for 1 min. The zinc powder charges negatively the surface of the substrate. Then, it attracts H_3O^+ ions and reduces them to H atoms which in turn reduce the Sn^{4+} ions, breaking up the conductive layer. The tape was removed and the glass washed under water flow, sonicated for 10 min in soap water, rinsed with distilled water, again sonicated for 10 min with acetone and rinsed with ethanol. The necessity to have a non conductive portion on the substrate comes from the method used to measure the cell efficiency, as described below. Using sol-gel and/or the deposition methods described above, the different material layers were deposited on these substrates (Fig. 3.7d). Deposition of

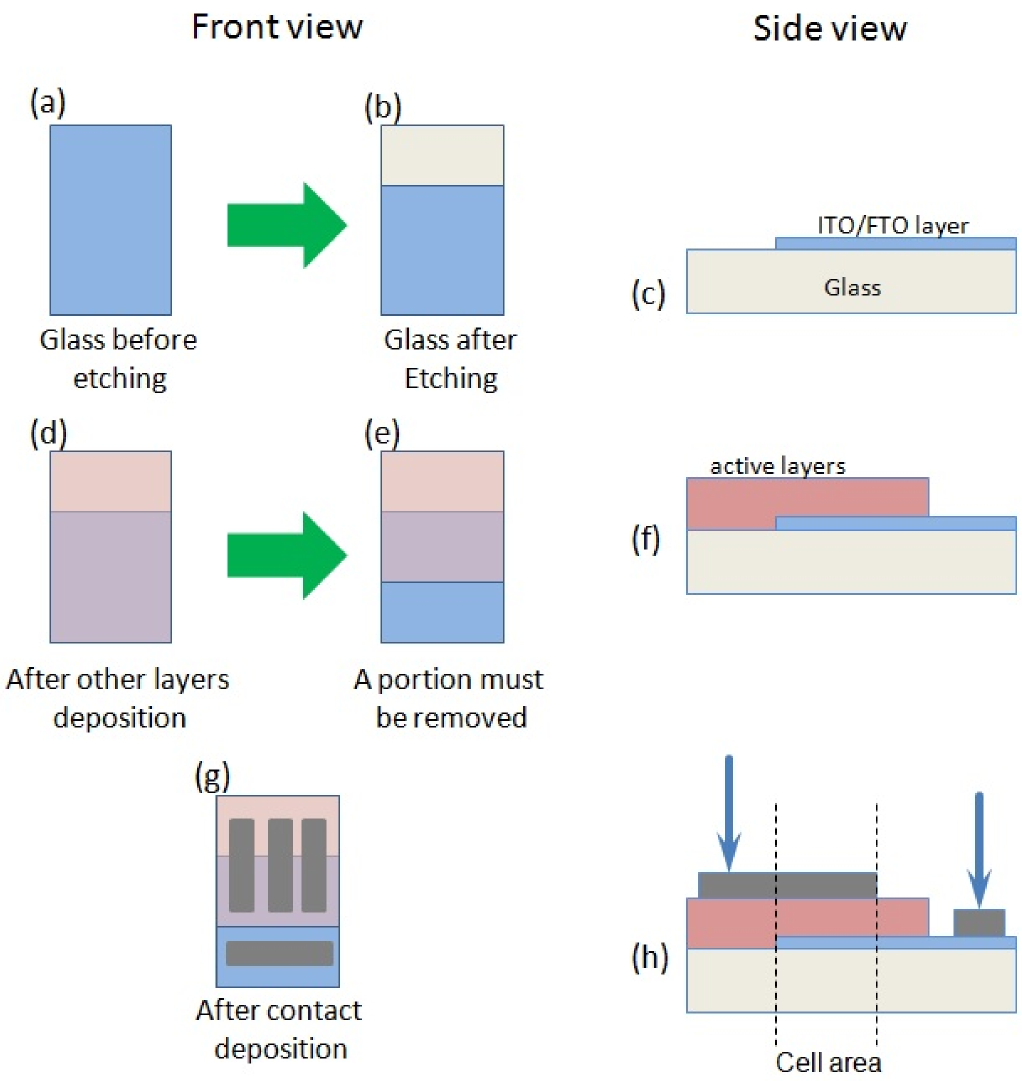

Fig. 3.7: Scheme of the manufacturing steps of the cell. In order are shown the glass (a) before and (b) after etching, the deposited material (d) before and (e) after the scratching and (g) the cell after metallic contact deposition; (c), (f) and (h) are the side views of the cell after (b), (e) and (g) steps respectively. (h) also indicates by arrows the position of the metallic tips during the measurements.

metallic contacts concludes the cell fabrication. These were made by thermal evaporation of the chosen metal using a mask, in order to have rectangular contacts positioned as shown in Fig. 3.7g. A thin layer of 3-5 nm of LiF or

MoO_3 was deposited before the 120-150 nm metallic layer, often silver. The presence of the salt improves the interface between the metal and the material below it, modifying their compatibility to facilitate the hole transport, acting also on the FF[95]. LiF was used mostly after the first attempts and for cells with Spiro-OMeTAD layers.

Before the contact deposition, a portion of the layers was scratched to expose the ITO or FTO glass. The horizontal contact was deposited on this portion while the three vertical ones are on top of the active layers. This architecture was chosen to reduce the probability of short circuit of the cell due to the needle shape of the metallic tips used for the measurement which could perforate soft materials and come in contact with the electrode below them, closing the circuit. Placing the tips on the non conductive portion of the glass (as shown in Fig. 3.7h) prevents this risk and the cell operation is preserved.

The actual solar cell is the portion of materials enclosed between the metallic contact and the conductive glass as shown, delimited by dashed lines, in Fig. 3.7h. This metallic architecture allows us to have three solar cells on the same substrate. In this way, it is possible to have, with less time and work, more statistical information about electrical parameters and efficiency of the cell.

3.3 Solar cell prototypes

Several attempts were performed starting from a simple architecture, based on PbS solar cell[96]. This cell is a BHJ where the active layer is mesoporous TiO_2 with PbS in its pores. The first attempt was therefore to replace the PbS with ligand exchanged HMS-sample nanoparticles. The following is the first architecture tested, made in collaboration with Dott. Petrozza and Mr.

Mazzotta from IIT (Italian Institute of Technology) in Milan.

On ITO glass, layers of compact and mesoporous TiO_2 were synthesized as described before. On top of TiO_2, a layer of Bi_2S_3 was deposited by dip coating, with the same parameters used during the preliminary test, three times. After each dipping step, the substrate was dipped into a solution of ethandithiol (EDT) 1 vol% in acetonitrile (ACN) for 120 sec and then in ACN for 30 sec to perform the ligand exchange. A final layer of 2,2´,7,7´-Tetrakis-(N,N-di-4-methoxyphenylamino)-9,9´-spirobifluorene (Spiro-OMeTAD) was deposited by spin coating (3000 rpm for 30 sec) followed by metallic contact put by thermal evaporation.

Contrary to its PbS-based analogous cell, this solar cell prototype does not produce a significant current and therefore its efficiency is almost zero. Anyway this was a first attempt and the starting point for the investigation on the causes of its inefficiency.

Initially it was noted that the TiO_2 films were characterized by macroscopic holes and opacity. These defects did not appear on the FTO substrates. It was attributed to a different wettability of the substrate which cannot be covered efficiently, causing defects on the final film. About the metallic contacts, aluminum, gold and silver were tested and at the end the silver was preferred. Also, another ligand exchange agent was tested on the Bi_2S_3 film. To replace the EDT, a TBAI solution in ethanol (1 mg/ml) was used, dipping the film 120 sec and then in ethanol for 30 sec obtaining similar result. It must be noted that TBAI is easier to handle and a safer compound than EDT.

Using scanning electron microscopy, SEM, all the layers of the cell became visible and it was also possible to measure their thickness. As visible in Fig. 3.8, the layer of Bi_2S_3 and TiO_2 are separated. Sulfide nanoparticles did not penetrate inside the pores and this means that not only the contact surface did not increase as we initially believed, but it could be reduced with respect to

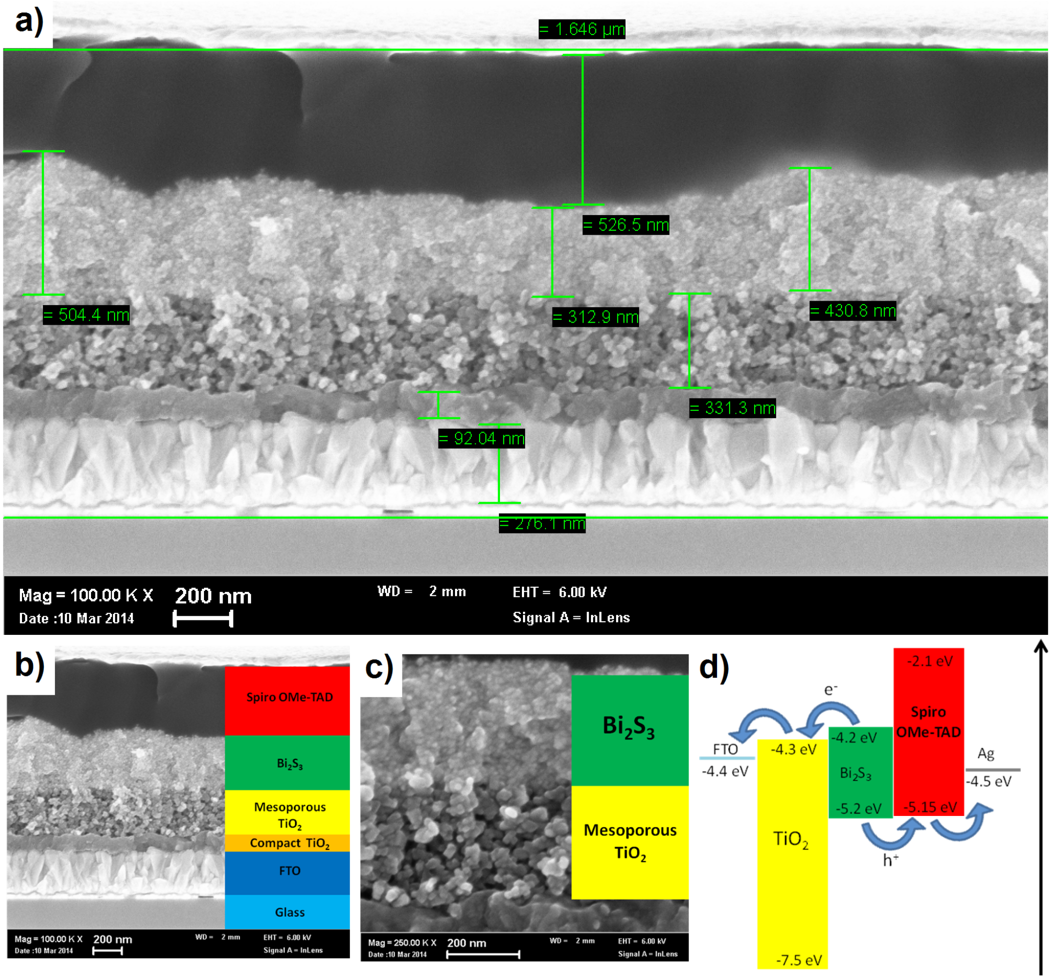

Fig. 3.8: (a,b) Side view SEM picture of the prototype with (c) a magnification on TiO_2-Bi_2S_3 layers.(d) Energy diagram of the bilayer cell prototype.[97,98]

a planar interface. To prove this fact, cells without mesoporous titania and titania-free were tested. The results are reported in Table 3.1. The absence of the mesopores does not influence the (poor) density of current, J_{sc}.

However, the presence of the mp-TiO_2 increases the Fill Factor (FF) causing a little higher efficiency. Complete removal of the titania from the cell causes the direct contact between FTO layer and bismuth sulfide with an increase of the J_{sc}. Unfortunately, V_{oc} and FF also decrease, and the final efficiency increases only up to the value of 0.0007%. For the sake of comparison,

Bi_2S_3-based cell prototypes	V_{oc} (V)	J_{sc} (mA/cm^2)	FF (%)	Efficiency (%)
With mp- and cp-TiO_2	0,26	0,0042	51,7	0,0006
With only cp-TiO_2	0,24	0,0043	36,6	0,0004
Without TiO_2	0,11	0,0201	32,6	0,0007
Without Bi_2S_3	0,52	0,0011	52,8	0,0003

Table 3.1: Cell parameters of Bi_2S_3-based cell variations tested.

the cell was tested also maintaining the titania but removing the Bi_2S_3. The result is a big increase of the V_{oc} but a sharp decrease of the J_{sc}, with a lower overall efficiency. It became clear that electrons can reach better the FTO electrode directly from the sulfide due to the absence of the resistance of the titania layers.

Bi_2S_3 appears necessary for the cell while TiO_2 looks to be more an obstacle than a good ETL, but this could be due to the interface between oxide and sulfide. Spiro-OMeTAD was then replaced by Poly(3-hexylthiophene-2,5-diyl) (P3HT), an organic conductive polymer that can also act as active layer[84,99]. Maintaining the same architecture used until now or removing only the mesoporous titania layer, the cell did not work (almost zero conversion efficiency). However, removing also the layer of compact titania, the efficiency increased to 0.04%, two orders of magnitude higher than before. This suggests, together with the first result obtained removing the Bi_2S_3, that an inadequate interaction between titania and sulfide was responsible for the poor efficiency and that the P3HT, working as active layer with the sulfide, could help improving the cell efficiency.

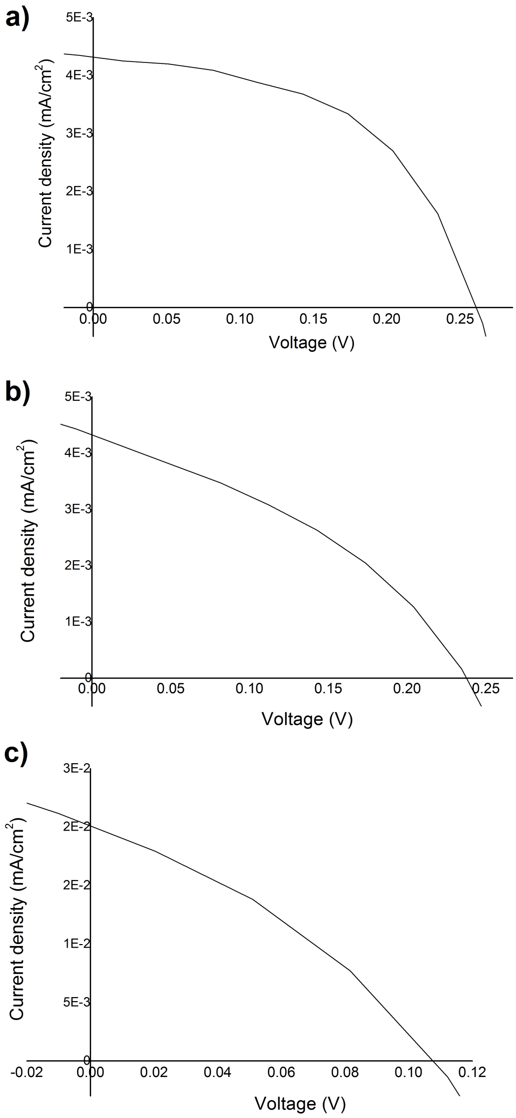

Fig. 3.9: J-V measurements of (a) FTO/cp-TiO_2/mp-TiO_2/Bi_2S_3/Spiro-OMeTAD/Ag, (b) FTO/cp-TiO_2/Bi_2S_3/Spiro-OMeTAD/Ag and (c) FTO/Bi_2S_3/Spiro-OMeTAD/Ag.

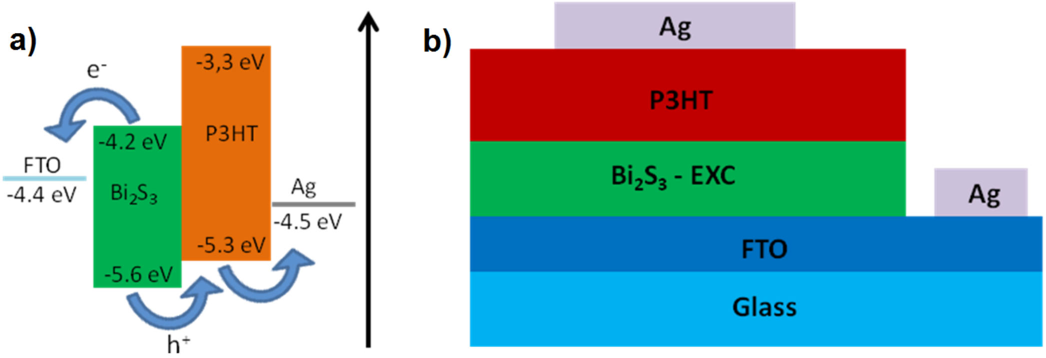

Fig. 3.10: (a) Energy diagram of bilayer P3HT/Bi_2S_3 solar cell compared with (b) a simple side view scheme of the device.

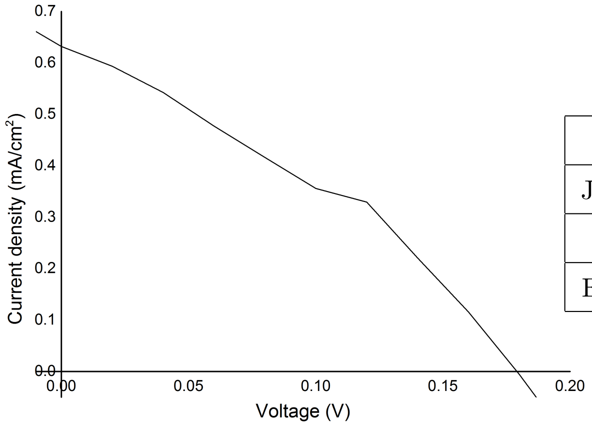

V_{oc} (V)	0,18
J_{sc} (mA/cm^2)	0,634
FF (%)	34,9
Efficiency (%)	0,04

Fig. 3.11: J-V measurement of bilayer P3HT/Bi_2S_3 solar cell and its parameters.

3.3.1 P3HT:Bi_2S_3 blend-based solar cell

Together with these observations, we started mixing the Bi_2S_3 nanoparticles with P3HT in a blend with a concentration of 50 mg/ml (70 wt% of nanoparticles) in toluene or chloroform, to try a new BHJ architecture. In this way, obviously, the contact surface is much larger than in the bilayer architecture because the nanoparticles are surrounded by P3HT, instead of being in contact only at the interface between two layers. A ligand exchange treatment has been performed in this case too, as suggested in literature, using ethanedithiol (EDT)[100]. Before use, the blend solution was maintained for minutes at 40°C stirring it with a magnetic stirrer, because it is a little viscous at room temperature. After the deposition on the substrate by spin coating (3000 rpm, 30 sec.), the film was dipped into a EDT 1 vol%. solution in acetonitrile (ACN) for 10 minutes and then rinsed with ACN.

The bulk heterojunction cell was tested with and without titania and also with and without bismuth sulfide. The results were similar to the bilayer cells and the cell with highest recorded efficiency, until now, did not have Bi_2S_3. The cells with mp-TiO_2 showed an increased efficiency if made by depositing P3HT without Bi_2S_3. In absence of the nanoparticles, the P3HT chains are free from the bond with the organic capping molecules and they can penetrate better inside the pores of the titania. At the same time, removing the mp-TiO_2 layer (so with only the cp-TiO_2 layer present), the efficiency is higher in presence of Bi_2S_3 nanoparticles with an improvement of the J_{sc} while the V_{oc} does not change significantly. The presence of Bi_2S_3, independently of cell architecture, reduces the V_{oc}. This suggests that the sulfide can work together with the P3HT as active layer but decreasing shunt resistances. It is clear that it is difficult for the charge carriers to be extracted from the active layer, and in particular from the Bi_2S_3, through the cell. The Bi_2S_3 is a material prone to sulfur vacancies and therefore with trap levels for the electrons that could be passivated by capping.

The alternatives to enhance the performance of these cells are two: to act on the ETL and HTL in order to force the charge carriers to move with higher efficiency or improve the interface between P3HT and bismuth sulfide, maybe through ligand exchange steps. For the first option it could be useful to look for some suitable materials to replace the one currently in use or modify its morphology acting on its quality, roughness or thickness.

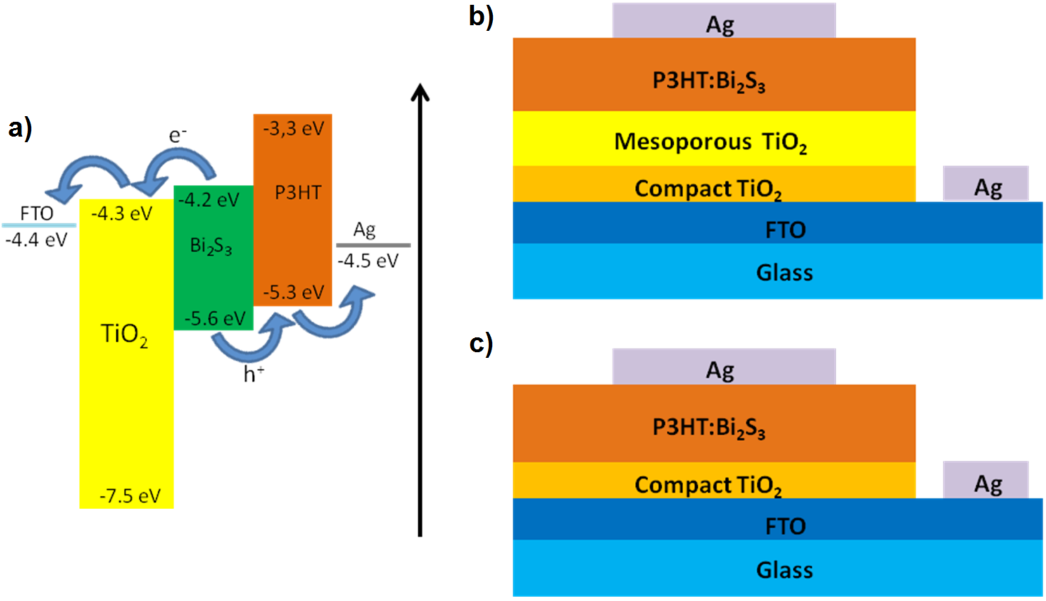

Fig. 3.12: (a) Energy diagram of BHJ P3HT:Bi_2S_3 blend-based solar cell compared with a simple side view scheme of the devices, (b) with and (c) without mp-TiO_2.

P3HT:Bi_2S_3 blend-based cells	V_{oc} (V)	J_{sc} (mA/cm^2)	FF (%)	Efficiency (%)
With mp- and cp-TiO_2	0,25	0,489	17,8	0,02
With mp- and cp-TiO_2 (Bi_2S_3-free)	0,59	0,915	35,0	0,19
With only cp-TiO_2	0,28	0,627	37,8	0,07
With only cp-TiO_2 (Bi_2S_3-free)	0,51	0,119	51,5	0,03

Table 3.2: Cell parameters of P3HT:Bi_2S_3 blend-based solar cell and its variations.

3.3.2 Alternative HTL

Beginning acting on the HTL/ETL, further attempts were done by replacing the final layer of P3HT of bilayer cells with poly(3,4-ethylenedioxythiophene) polystyrene sulfonate (PEDOT:PSS), another polymeric HTL. During the PEDOT:PSS deposition by spin coating, the cell was irreparably damaged. Decreasing the numbers of used PEDOT:PSS solution drops, instead, maintained the cell intact but always short-circuited. The reason became clear observing the samples by optical microscopy. The surface of the cell was characterized by the presence of several cracks so the metallic contact evaporated at the end penetrate the layers, short-circuiting the cell. The PEDOT:PSS, when dried on the surface of the cell because of the spinning, bonds strongly with the layers below and contract itself. The results are large cracks that allow the metallic contact to get in touch with the electrode below. Higher concentrations of PEDOT:PSS cause also the rolling of the layer, forming a black powder and wide cracks visible by naked eyes, as shown by optical microscopy pictures of Fig. 3.13.

Considering these results, instead of an HTL layer that would cover completely the layer below it, a thin layer of MoO_3 was added only on the area between the P3HT and the silver contacts, replacing the LiF. This oxide could work as p-dopant[101] and give similar performance of a PEDOT:PSS hole transport layer[102]. Similarly to LiF, the MoO_3 might further facilitate the hole transport from the P3HT (native p-type) to the electrode, modifying their interface and reducing the possibility of penetration of Ag atoms into the layer underneath.

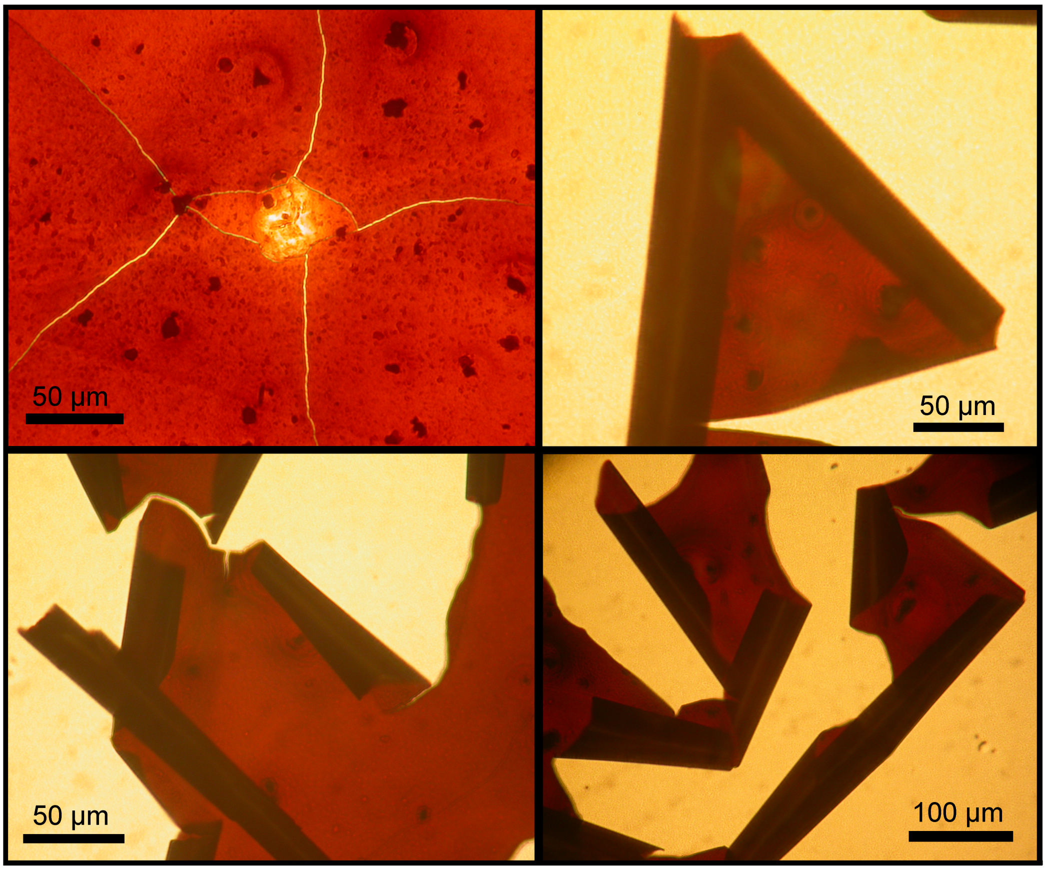

Fig. 3.13: Optical microscopy pictures of prototypes with a final layer of PEDOT:PSS. Picture on top-left shows large cracks, the others show the rolls. Brown color is due to the Bi_2S_3 layer.

3.3.3 Alternative ETL

Looking for alternatives to titania, zinc oxide appears to be a good candidate. Its similar energy gap and transparence as film could be useful for an application in this field[84]. At the same time, aluminum doped zinc oxide, AZO, has a three orders of magnitude higher conductivity than ZnO, due to the n-type doping, with a very similar energy gap, only 0,06 eV higher[103,104]. As TiO_2 did not produce a good film on the ITO glasses, ZnO and AZO showed a similar problem on FTO glasses, but this time visible also by naked eye. First attempts using FTO, in fact, did not produce results. Replacing the FTO with ITO the cells did work again. This is probably due to poor wettability of the substrate by the ZnO and AZO sol.

Starting from an architecture proposed by Konstantatos et al.[24] that reports a Bi_2S_3:P3HT blend-based solar cell with a efficiency of 1%, a further architecture has been tested. Its scheme is shown in Fig. 3.14. ZnO or AZO were the ETL of the cell. With the same role, a thin layer of Bi_2S_3 is used as interface between zincite and Bi_2S_3:P3HT blend. A final layer of P3HT plays the role of HTL.

One drop of colloidal Bi_2S_3 (not less than 20 mg/ml in toluene) was deposited on the glass while spinning at 2000 rpm. Six to eight drops of EDT 2 vol% in ACN were dropped on the static film and let react for 20-30 seconds. Then, the substrate was rinsed with ACN and toluene flush. This process was repeated three time to obtain a film of 50-60 nm.

Few drops of P3HT/Bi_2S_3 blend 50 mg/ml (70% of nanoparticles) in chloroform was deposited in the center of the glass and then spun at 3000 rpm. Ligand exchange treatments have been performed by dipping the film into an EDT 1 vol% in ACN bath for 10 min, rinsed with 1:1 ACN/ethylacetate mixture and dried under nitrogen atmosphere. After that, an annealing step at 110°C for 7 minutes in air was done. When necessary, a second layer was spin-cast, dropping the solution on the substrate already rotating, not to damage the layer below. The same ligand exchange treatment has been done, followed by the annealing step. At the end, a drop of P3HT (50 mg/ml in chlorobenzene) has been deposited while spinning at 3000 rpm and then annealed at 110°C for 7 minutes.

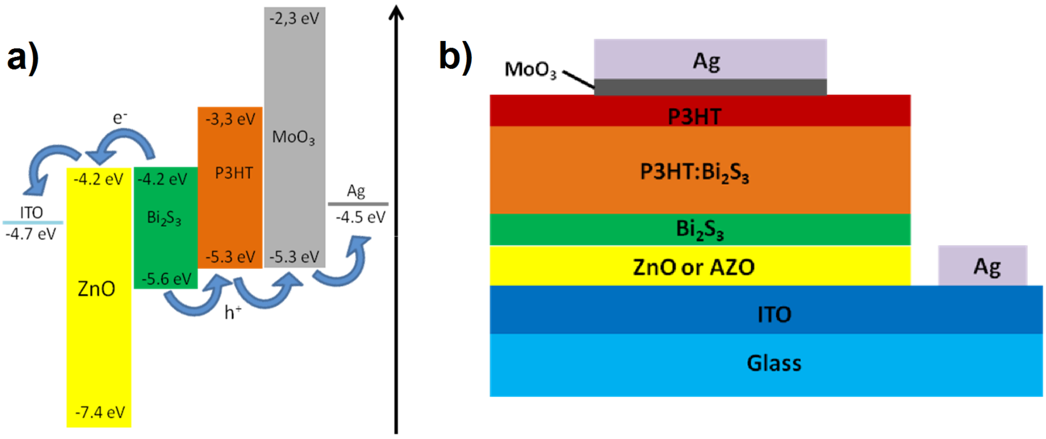

Fig. 3.14: (a) Energy diagram of BHJ P3HT:Bi_2S_3 blend-based solar cell compared with (b) a simple side view scheme of the device.

The prototype made with ZnO as ETL showed a maximum efficiency of 0,13% that rose up to 0,25% using the AZO, with a good increase of the J_{sc}. The V_{oc} instead is quite similar while the FF decreases slightly. These values are markedly lower than reports in literature for the same architecture using ZnO of an efficiency of 1%, shown by Konstantatos et al.[22,24,43]. The difference between the literature and our cells could depend on various factors: the quality of the materials, instrument and solvent used, quality of produced films. At the moment, comparable values to the ones reported by Konstantatos et al. have not been demonstrated by other authors during the writing of this thesis.

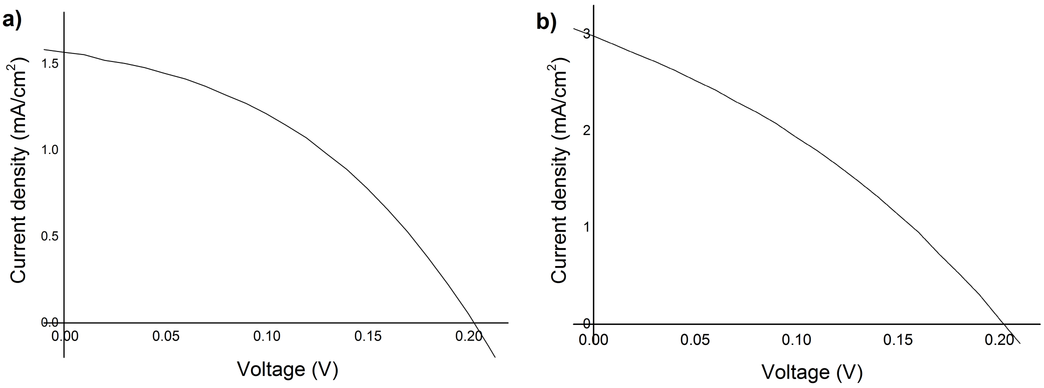

Fig. 3.15: J-V measurements of BHJ P3HT/Bi_2S_3 blend-based solar cell with (a) ZnO or (b) AZO as ETL.

Blend-based BHJ solar cell	V_{oc} (V)	J_{sc} (mA/cm^2)	FF (%)	Efficiency (%)
With ZnO	0,20	1,568	40,5	0,13
With AZO	0,23	3,023	35,5	0,25

Table 3.3: Cell parameters of BHJ P3HT/Bi_2S_3 blend-based solar cell with ZnO or AZO as ETL

3.3.4 Alternative ligand exchange agent and thickness

It is difficult to understand how effective was the ligand exchange treatment on the blend. Usually, a FT-IR measurement would be carried out to see variations of characteristic signals of the capping organic molecules chains, but results in our case were indistinguishable from the signals of the P3HT.

Tetrabutylammonium iodide (TBAI) was used as exchange agent both for Bi_2S_3 and blend ligand exchange steps instead of EDT. After the treatment, performed with the same method described before, the efficiency increases until a maximum recorded value of about 0,38%. When TBAI is used only for the ligand exchange step on the blend, so maintaining the EDT as exchange agent for the Bi_2S_3 layer, the efficiency decreases slightly.

Blend-based BHJ with AZO	V_{oc} (V)	J_{sc} (mA/cm^2)	FF (%)	Efficiency (%)
Exchanged with EDT and TBAI	0,28	3,327	38,5	0,36
Exchanged with only TBAI	0,34	2,704	40,8	0,38

Table 3.4: Cell parameters of BHJ P3HT/Bi_2S_3 blend-based solar cell EDT/TBAI or only TBAI ligand exchanged.

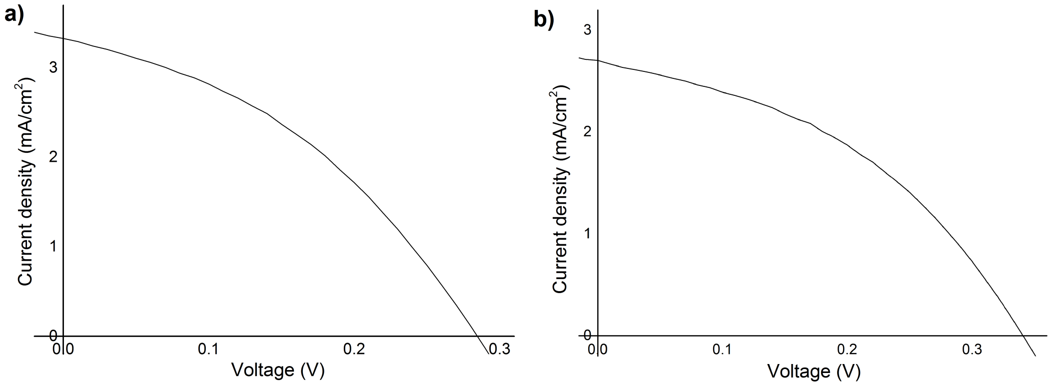

Fig. 3.16: J-V measurements of BHJ solar cell with AZO as ETL (a) which ligand exchange performed with EDT and TBAI and (b) with only TBAI.

Other attempts were performed acting on Bi_2S_3 and P3HT layers thickness or presence. Reducing the thickness of the P3HT layer using a higher spinning speed, for example 7000 rpm instead of 3000 rpm, enhances a little the J_{sc} but with a lower FF. Removing the Bi_2S_3 ETL, the efficiency of the cell decreases due mostly to the decrease of the FF. The Bi_2S_3-free cell, made only by AZO and P3HT in a bilayer architecture, showed a good increase of V_{oc} and FF, in agreement with the data reported in previous sections, but the J_{sc} decreased by one order of magnitude and the efficiency with it. This is a further demonstration of how the Bi_2S_3 is useful for the proper operation of this type of solar cells.

Blend-based BHJ with AZO	V_{oc} (V)	J_{sc} (mA/cm^2)	FF (%)	Efficiency (%)
Exchanged only with TBAI (*)	0,34	2,704	40,8	0,38
* with thin P3HT HTL layer	0,33	3,263	28,4	0,30
* without Bi_2S_3 ETL layer	0,35	1,717	32,3	0,19
* with thin P3HT HTL layer and without Bi_2S_3ETL layer	0,34	2,339	34,3	0,27
* Bi_2S_3-free	0,55	0,329	43,4	0,08

Table 3.5: Cell parameters from J-V measurements of blend-based BHJ with AZO variations and Bi_2S_3-free cells.

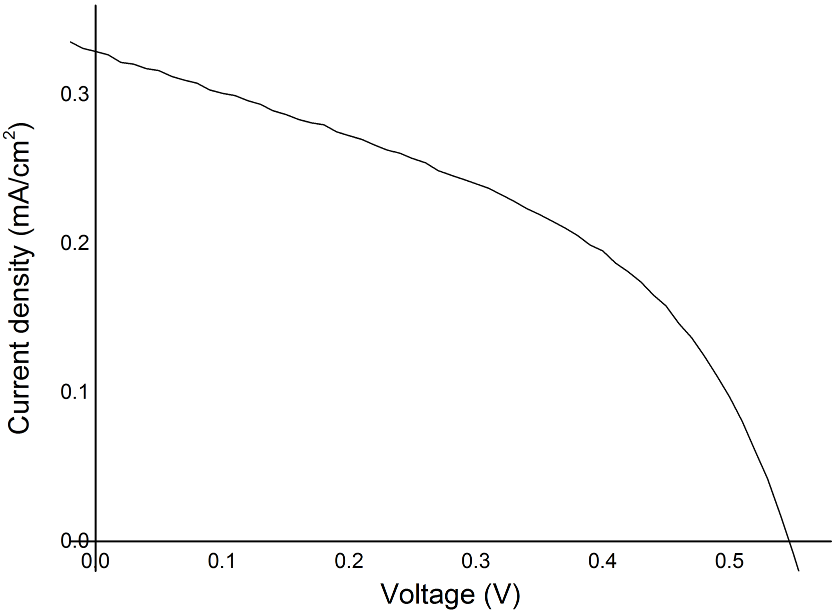

Fig. 3.17: J-V measurement of bilayer AZO/P3HT solar cell.

3.4 Conclusions

Currently, the highest efficiency shown in literature for Bi_2S_3-based solar cell is 1.1%[24], virtually unchanged from three years[22,24,43] and no other research groups (during the writing of this thesis) have published similar results. On the other hand, the highest value reached during this work has been 0,4%. These facts make the bismuth sulfide not competitive with respect of other materials like perovskites or other heavy metals chalcogenides. PbS-based solar cells, for example, started from an efficiency value of 0,49% in 2002[96] to 5,2% in 2013[17]. Hybrid perovskite-based solar cells have seen a growth from 3,8%[105] to around 20% in 7 years, but with a fast increase from 15% to 20% in the last two[106].

Even if the final efficiencies were not comparable with the results shown in literature with similar materials, the Bi_2S_3 appears to be an active component of these solar cells anyway. Its absence increases the V_{oc} but decrease greatly the J_{sc}. This fact could be a proof of the role played by this sulfide as active material and it is also in agreement with its optoelectronic properties. As shown in Chapter 2, Bi_2S_3 lattice tents naturally to have sulfur vacancies[30,47] that, through relaxation effects, could saturate shallow traps. In fact, it has been demonstrated that a large fraction of photoexcited electrons are not trapped by the nanoparticles while the holes are quickly captured by midgap states[30]. For this reason, the presence of Bi_2S_3 can increase the density of current but causing also the negative effect on V_{oc} observed. Looking at optical properties of this sulfide, it appears to be a good light absorber (see Chapter 2). This fact suggests a better application not as main active material but in combination with another n-type material.

An organic capping should at least reduce the presence of midgap states[47] but in the end, also when the nanoparticles have been synthesized by colloidal method, it does not seem to be effective enough. Exchange of the native capping from the synthesis with a different type before the deposition on the substrate has proved counterproductive; doing it after the deposition, instead, was effective and it has been possible to observe a true substitution of the chain capping molecules with the shorter ones. The thiol group (-SH) of the EDT can react with the sulfide surface, replacing its bond with the oleic acid functional groups with disulfide bridges (-S-S-). Furthermore, the EDT can give a p-type conductivity contributions to PbS nanoparticles[107,108]. Particularly, an improvement in the interaction between the chalcogenides and the organic HTL was expected to promote charge conduction. We determined this strategy to be not so effective. Contrary to the EDT, TBAI gives a n-type contribute to the chalcogenide nanoparticles[107,108]. This organic salt turned out to be more effective in improving the solar cell parameters, increasing the efficiency and making the cell building process safer for the operators. Similar benefits of using TBAI as exchange agent have been observed also for bilayer solar cells but without comparable efficiencies of BHJ cells.

Another source of issues for the proper functioning of the solar cell prototype is its complexity. The higher the number of materials involved for the cell, the larger will be the number of interfaces and also the probability to have defects on them. In fact each layer of material needs appropriate treatments as thermal annealings or ligand exchanges. The architecture of the cell must be studied also considering the order and type of material used not only based on the affinity between energy levels but also on their chemical-physical characteristics. Materials like Bi_2S_3, for example, cannot be treated at the same high temperature needed for TiO_2 or ZnO formation. So, in conclusion, the high number of steps involved for the manufacturing of the device could be partly responsible for its poor performance.

Chapter 4

Conclusions

Bismuth sulfide (Bi_2S_3) is considered a good candidate for applications in third generation solar cells, especially in substitution of chemically similar but toxic heavy metal chalcogenides. The main aim of this work has been to explore the possibility to tune structural and morphological properties of this material and its contribution to solar cell operation and development.

Surfactant-assisted colloidal synthesis has proved to be an effective method for the production of bismuth sulfide nanoparticles with controlled size, shape and with the possibility to disperse them into various solvents. The control on size and colloidal stability have been revealed important for the subsequent application in solution-processable devices. The use of hexamethyldisilathiane (HMS) and elemental sulfur powder in oleylamine (OAm) solution, as chalcogen precursors, allowed to obtain pure nanocrystalline Bi_2S_3 with orthorhombic lattice and variable colloidal stability. OAm acts on the kinetics of the reactions involved, accelerating the synthesis and forcing the nanoparticles growth along their [001] crystallographic direction. This property allowed us to vary the morphology of the particles from spherical to rod shaped and ultrathin nanowires. The wires displayed some morphological defects but could be an ideal starting point for the development of crystalline ultrathin nanowires, that are expected to be energetically stable at room temperature by theoretical simulations[47]. Optical properties of each sample produced results comparable to the literature, as demonstrated by UV-Visible absorption spectroscopy, and no photoluminescence has been observed.

First attempts with a totally inorganic bulk heterojunction (BHJ) solar cell based on Bi_2S_3 and mesoporous TiO_2 did not give good results due to their poor solar photoconversion efficiency and poor interaction between materials at their interfaces. Bilayer and BHJ architecture using P3HT as p-type semiconductor allows to build a hybrid solar cell that gave better results, particularly when used in blend with the nanoparticles. The best efficiency value has been obtained with a hybrid BHJ with aluminum doped zinc oxide and a thin layer of Bi_2S_3 as ETL, a blend of Bi_2S_3 nanoparticles in P3HT as active layer and P3HT as HTL; the electrodes were made of indium tin oxide on glass support, for the directly illuminated area, and MoO_3 and silver contact on the opposite side. Bi_2S_3 appears to be, for its n-type nature and its effects on V_{oc} and J_{sc} of the cell, a good material as electron transport layer but not so good for the active layer of the cell. Its inclination to trap holes into midgap states but also to release photoexcited electrons are promising feature for solar cell architectures.

List of Figures

List of Tables

Bibliography

[1] International Energy Agency. *Key World Energy Statistics*. Chirat, 2014.

[2] International Energy Agency. *World Energy Outlok*. CORLET, 2014.

[3] M. King Hubbert. Nuclear energy and the fossil fuel. *Drilling and Production Practice*, 1956.

[4] British Petroleum. *Statistical Review of World Energy*. Pureprint Group, 2015.

[5] NASA. *Scientific evidence for warming of the climate system is unequivocal*. http://climate.nasa.gov/evidence/, 2015.

[6] NASA. *Carbon Dioxide, latest measurement: Sep 2015*. http://climate.nasa.gov/vital-signs/carbon-dioxide/, 2015.

[7] T.F. Stocker, D. Qin, G.K. Plattner, M. Tignor, S.K. Allen, J. Boschung, A. Nauels, Y. Xia, V. Bex, and P.M. Midgley. *Climate Change 2013: The Physical Science Basis. Contribution of Working Group I to the Fifth Assessment Report of the Intergovernmental Panel on Climate Change*. Cambridge University Press, Cambridge, United Kingdom and New York, NY, USA, 2013.

[8] C.W. Li, J. Ciston, and M.W. Kanan. Electroreduction of carbon monoxide to liquid fuel on oxide-derived nanocrystalline copper. *Nature*, 508, 2014.

[9] U.S. Energy Information Administration. *Levelized Cost and Levelized Avoided Cost of New Generation Resources in the Annual Energy Outlook 2015.* Independent Statistics & Analysis, 2015.

[10] H. Sharman, B. Leyland, and M. Livermore. *Renewable Energy Vision or Mirage?* Grosvenor Group (Print Services), 2011.

[11] Y.-F. Chiang, R.-T. Chen, P.-S. Shen, P. Chen, and T.-F. Guo. Extension lifetime for dye-sensitized solar cells through multiple dye adsorption/desorption process. *Journal of Power Sources*, 225(257-262), 2013.

[12] Michael Grätzel. The advent of mesoscopic injection solar cells. *Prog. Photovolt: Res. Appl.*, 14:429–442, 2006.

[13] Christoph J. Brabec. Organic photovoltaics:technology and market. *Solar Energy Materials & Solar Cells*, 83:273–292, 2004.

[14] A.D. McNaught and A. Wilkinson. Compendium of chemical terminology: IUPAC recommendations (2nd ed.). *Blackwell Science*, 1997.

[15] W. Shockley and H.J. Queisser. Detailed balance limit of efficiency of p-n junction solar cells. *Journal of Applied Physics*, 32(3), 1960.

[16] C. Wadia, A.P. Alivisatos, and D.M. Kammen. Materials availability expands the opportunity for large-scale photovoltaics deployment. *Environ. Sci. Technol.*, 43:2072–2077, 2009.

[17] C. Piliego, L. Protesescu, S.Z. Bisri, M.V. Kovalenko, and M.A. Loi. 5.2% efficient PbS nanocrystal Schottky solar cells. *Energy Environ. Sci.*, 6(3054), 2013.

[18] D.V. Talapin, J.S. Lee, M.V. Kovalenko, and E.V. Shevchenko. Prospects of colloidal nanocrystals for electronic and optoelectronic applications. *Chem. Rev.*, 110:389–458, 2010.

[19] M. V. Kovalenko, L. Manna, A. Cabot, Z. Hens, D.V. Talapin, C.R. Kagan, V.I. Klimov, A.L. Rogach, P. Reiss, D.J. Milliron, P. Guyot-Sionnnest, G. Konstantatos, W.J. Parak, T. Hyeon, B.A. Korgel, C.B. Murray, and W. Heiss. Prospects of nanoscience with nanocrystals. *ACS Nano*, 9(2):1012–1057, 2015.

[20] K.C. Staudinger and V.S. Roth. Occupational lead poisoning. *Am. Fam. Physician*, 4(57):719–726, 1998.

[21] W. Maret and J.M. Moulis. The bioinorganic chemistry of cadmium in the context of its toxicity. *Metal Ions in Life Sciences*, 11:1–29, 2012.

[22] A.K. Rath, M. Bernechea, L. Martinez, F.P. G. de Arquer, J. Osmond, and G. Konstantatos. Solution-processed inorganic bulk nano-heterojunctions and their application to solar cells. *Nat. Photonics*, 529(6), 2012.

[23] Z. Wang, S. Qu, X. Zeng, J. Liu, F. Tan, L. Jin, and Z. Wang. Influence of interface modification on the performance of polymer/ Bi_2S_3 nanorods bulk heterojunction solar cells. *Appl. Surf. Sci.*, 257(2):423–428, 2010.

[24] L. Martinez, A. Stavrinadis, S. Higuchi, S. L. Diedenhofen, M.Bernechea, K. Tajima, and G. Konstantatos. Hybrid solution-processed bulk heterojunction solar cells based on bismuth sulfide nanocrystals. *Phys.Chem. Chem. Phys.*, 15(5482), 2013.

[25] Q. Guo, H.W. Hillhouse, and R. Agrawal. Synthesis of Cu_2ZnSnS_4 nanocrystal ink and its use for solar cells. *J Am Chem Soc.*, 33(131):11672–11673, 2009.

[26] J. Tang and A.P. Alivisatos. Crystal splitting in the growth of Bi_2S_3. *Nano Lett.*, 6(12), 2006.

[27] J.M. Kinsella, R.E. Jimenez, P.P. Karmali, A.M. Rush, V. R. Kotamraju, N.C. Gianneschi, E. Ruoslahti, D. Stupack, and M.J. Sailor. X-ray computed tomography imaging of breast cancer by using targeted peptide-labeled bismuth sulfide nanoparticles. *Angew. Chem.*, 50:12308–12311, 2011.

[28] J. Liu, X. Zheng, L. Yan, L. Zhou, G. Tian, W. Yin, L. Wang, Y. Liu, Z. Hu, Z. Gu, C. Chen, and Y. Zhao. Bismuth sulfide nanorods as a precision nanomedicine for in vivo multimodal imaging-guided photothermal therapy of tumor. *ACS Nano*, 9:696–707, 2015.

[29] J. Chen, X.-Q. Yang, Y.Z. Meng, H.H. Huang, M.Y. Qin, D.-M. D.M. Yan, Y.D. Zhao, and Z.Y. Ma. In vitro and in vivo CT imaging using bismuth sulfide modified with a highly biocompatible Pluronic F127. *Nanotechnology*, 25, 2014.

[30] M. Aresti, M. Saba, **R. Piras**, D. Marongiu, G. Mula, F. Quochi, A. Mura, C. Cannas, M. Mureddu, A. Ardu, G. Ennas, V. Calzia, A. Mattoni, A. Musinu, and G. Bongiovanni. Colloidal Bi_2S_3 nanocrystals: Quantum size effects and midgap states. *Adv. Funct. Mater.*, 24:3341–3350, 2014.

[31] R. Caracas and X. Gonze. First-principles study of the electronic properties of A_2B_3 minerals, with A=Bi,Sb and B=S,Se. *Phys Chem Minerals*, 32:295–300, 2005.

[32] L.F. Lundegaard, E. Makovicky, T. Boffa-Ballaran, and T. Balic-Zunic. Crystal structure and cation lone electron pair activity of Bi_2S_3 between 0 and 10 GPa. *Phys Chem Minerals*, 32:578–584, 2005.

[33] A.A. Tahir, M.A. Ehsan, M. Mazhar, K.G.U. Wijayantha, M. Zeller, and A.D Hunter. Photoelectrochemical and photoresponsive properties of Bi_2S_3 nanotube and nanoparticle thin films. *Chem. Mater.*, 22:5084–5092, 2010.

[34] V. Calzia, G. Malloci, G. Bongiovanni, and A. Mattoni. Electronic properties and quantum confinement in Bi_2S_3 ribbon-like nanostructures. *J. Phys. Chem. C*, 117:21923–21929, 2013.

[35] Y. Sharma, P. Srivastava, A. Dashora, L. Vadkhiya, M. Bhayani, R. Jain, A. Jani, and B. Ahuja. Electronic structure, optical properties and Compton profiles of Bi_2S_3 and Bi_2Se_3. *Solid State Sci.*, 14(241-249), 2012.

[36] M.R. Filip, C.E. Patrick, and F. Giustino. GW quasiparticle band structures of stibnite, antimonselite, bismuthinite and guanajuatite. *Phys. Rev. B: Condens. Matter Mater. Phys.*, 87(205125), 2013.

[37] H. Koc, H. Ozisik, E. Deligöz, A.M. Mamedov, and E. Ozbay. Mechanical, electronic and optical properties of Bi_2S_3 and Bi_2Se_3 compounds: first principle investigations. *J. Mol. Model.*, 20(2180), 2014.

[38] N. Yesugade, C. Lokhande, and C. Bhosale. Structural and optical properties of electrodeposited Bi_2S_3, Sb_2S_3 and As_2S_3 thin films. *Thin Solid Films*, 263(145-149), 1995.

[39] J. Lukose and B. Pradeep. Electrical and optical properties of bismuth sulphide [Bi_2S_3] thin films prepared by reactive evaporation. *Solid State Commun.*, 78(535-538), 1991.

[40] S. Mahmoud, A.H. Eid, and H. Omar. Optical characteristics of bismuth sulfide (Bi_2S_3) thin films. *Fizika A*, 6(111-120), 1997.

[41] X. Yu, C. Cao, and H. Zhu. Synthesis and photoluminescence properties of Bi_2S_3 nanowires via surfactant micelle-template inducing reaction. *Solid State Communications*, 134:239–243, 2005.

[42] B. Miller and A. Heller. Semiconductor liquid junction solar cells based on anodic sulphide films. *Nature*, 262, 1976.

[43] G. Konstantatos, L. Levina, J. Tang, and E.H. Sargent. Sensitive solution-processed Bi_2S_3 nanocrystalline photodetectors. *Nano Lett.*, 4002(8):4002–4006, 2008.

[44] A. K. Rath, M. Bernechea, L. Martinez, and G. Konstantatos. Solution-processed heterojunction solar cells based on p-type PbS quantum dots and n-type Bi_2S_3 nanocrystals. *Adv. Mater.*, 6:529–534, 2011.

[45] L. Martinez, M. Bernechea, F.P. G. de Arquer, and G. Konstantatos. Near IR-sensitive, non-toxic, polymer/nanocrystal solar cells employing Bi_2S_3 as the electron acceptor. *Adv. Energy Mater.*, 1:1029–1035, 2011.

[46] L. Martinez, S. Higuchi, A.J. MacLachlan, A. Stavrinadis, N.C. Miller, S.L. Diedenhofen, M. Bernechea, S. Sweetnam, J. Nelson, S.A. Haque, K. Tajima, and G. Konstantatos. Improved electronic coupling in hybrid organic-inorganic nanocomposites employing thiol-functionalized P3HT and bismuth sulfide nanocrystals. *Nanoscale*, 6(10018-10026), 2014.

[47] V. Calzia, **R. Piras**, A. Ardu, A. Musinu, M. Saba, G. Bongiovanni, and A. Mattoni. Atomistic modeling of morphology and electronic properties of colloidal ultrathin Bi_2S_3 nanowires. *J. Phys. Chem. C*, 119(29):16913–16919, 2015.

[48] C.J. Tang, G.Z. Wang, H.Q. Wang, Y.X. Zhang, and G.H. Li. Facile synthesis of Bi_2S_3 nanowire arrays. *Materials Letters*, 62:3663–3665, 2008.

[49] L. Cademartiri, R. Malakooti, P.G. O'Brien, A. Migliori, S. Petrov, N.P. Kherani, and G.A. Ozin. Large-scale synthesis of ultrathin Bi_2S_3 necklace nanowires. *Angew. Chem.*, 47:3814–3817, 2008.

[50] H.C. Liao, M.C. Wu, M.H. Jao, C.M. Chuang, Y.F. Chend, and W.F. Su. Synthesis, optical and photovoltaic properties of bismuth sulfide nanorods. *CrystEngComm*, 14:3645–3652, 2012.

[51] G. Xiao, Q. Dong, Y. Wang, Y. Sui, J. Ning, Z. Liu, W. Tian, B. Liu, G. Zoua, and B. Zou. One-step solution synthesis of bismuth sulfide (Bi_2S_3) with various hierarchical architectures and their photoresponse properties. *RSC Adv.*, 2:234–240, 2012.

[52] M. Ibañez, P. Guardia, A. Shavel, D. Cadavid, J. Arbiol, J.R. Morante, and A. Cabot. Kinetics of asymmetric Bi_2S_3 nanocrystals: Size distribution focusing in nanorods. *J. Phys. Chem.C*, 115:7947–7955, 2011.

[53] S. Shen, Y. Zhang, L. Peng, B. Xu, Y. Du, M. Deng, H.i Xu, and Q. Wang. Generalized synthesis of metal sulfide nanocrystals from single-source precursors: size, shape and chemical composition control and their properties. *CrystEngComm*, 13:4572–4579, 2011.

[54] P.K. Nair, M.T.S. Nair, V.M. García, O.L. Arenas, Y. Peña, A. Castillo, I.T. Ayala, O. Gomezdaza, A. Sánchez, J. Campos, H. Hu, R. Suárez, and M.E. Rincón. Semiconductor thin films by chemical bath deposition for solar energy related applications. *Solar Energy Materials and Solar Cells*, 52(3):313–344, 1998.

[55] R.I. Walton. Subcritical solvothermal synthesis of condensed inorganic materials. *Chem. Soc. Rev.*, 31:230–238, 2002.

[56] Y. Yin and A.P. Alivisatos. Colloidal nanocrystal synthesis and the organic-inorganic interface. *Nature*, 437:664–670, 2005.

[57] L.M. Peter, K.G.U. Wijayantha, D.J. Riley, and J.P. Waggett. Band-edge tuning in self-assembled layers of Bi_2S_3 nanoparticles used to photosensitize nanocrystalline TiO_2. *J. Phys. Chem. B*, 107:8378–8381, 2003.

[58] Z. Quan, J. Yang, P. Yang, Z. Wang, C. Li, and J. Lin. Facile synthesis and characterization of single crystalline Bi_2S_3 with various morphologies. *Cryst. Growth Des.*, 8:200–207, 2008.

[59] B. Xue, T. Sun, F. Mao, and J. Xie. Gelatin-assisted green synthesis of bismuth sulfide nanorods under microwave irradiation. *Mater. Lett.*, 122:106–109, 2014.

[60] Z. Chen and M. Cao. Synthesis, characterization, and hydrophobic properties of Bi_2S_3 hierarchical nanostructures. *Mater. Res. Bull.*, 46:555–562, 2011.

[61] J. Jiang, S.H. Yu, W.T. Yao, H. Ge, and G.Z. Zhang. Morphogenesis and crystallization of Bi_2S_3 nanostructures by an ionic liquid-assisted templating route: synthesis, formation mechanism, and properties. *Chem. Mater.*, 17:6094–6100, 2005.

[62] M.A. Hines and G.D. Scholes. Colloidal PbS nanocrystals with size-tunable near-infrared emission: Observation of post-synthesis self-narrowing of the particle size distribuion. *Adv. Matet.*, 15(21), 2003.

[63] H. Li, D. Chen, L. Li, F. Tang, L. Zhanga, and J. Rena. Size and shape-controlled synthesis of PbSe and PbS nanocrystals via a facile method. *CrystEngComm*, 12:1127–1133, 2010.

[64] **R. Piras**, M. Aresti, M. Saba, D. Marongiu, G. Mula, F. Quochi, A. Mura, C. Cannas, M. Mureddu, A. Ardu, G. Ennas, V. Calzia, A. Mattoni, A. Musinu, and G. Bongiovanni. Colloidal synthesis and

characterization of Bi_2S_3 nanoparticles for photovoltaic applications. *Journal of Physics: Conference Series*, 566(012017), 2014.

[65] J.W. Thomson, L. Cademartiri, M. MacDonald, S. Petrov, G. Calestani, P. Zhang, and G.A. Ozin. Ultrathin Bi_2S_3 nanowires: Surface and core structure at the cluster-nanocrystal transition. *J. Am. Chem. Soc.*, 132:9058–9068, 2010.

[66] L. Lutterotti, S. Matthies, and H.-R. Wenk. Maud (material analysis using diffraction): a user friendly java program for rietveld texture analysis and more. *Proceeding of the Twelfth International Conference on Textures of Materials (ICOTOM-12)*, 1(1599), 1999.

[67] C. John. *Interpretation of infrared spectra, a practical approach.* R.A. Meyers, 2000.

[68] C. Cannas, A. Musinu, A. Ardu, F. Orr, D. Peddis, M. Casu, R. Sanna, F. Angius, G. Diaz, and G. Piccaluga. $CoFe_2O_4$ and $CoFe_2O_4/SiO_2$ core/shell nanoparticles: Magnetic and spectroscopic study. *Chem. Mater.*, 22:3353–3361, 2010.

[69] L.M. Bronstein, X. Huang, J. Retrum, A. Schmucker, M. Pink, B.D. Stein, and B. Dragnea. Influence of iron oleate complex structure on iron oxide nanoparticle formation. *Chem. Mater.*, 19:3624–3632, 2007.

[70] J. Park, K. An, Y. Hwang, J.G. Park, H.J. Noh, J.Y. Kim, J.H. Park, N.M. Hwang, and T. Hyeon. Ultra-large-scale syntheses of monodisperse nanocrystals. *Nature Materials*, 3:891–895, 2004.

[71] C. Cara, A. Musinu, V. Mameli, A. Ardu, D. Niznansky, J. Bursik, M. Casu, A. Scorciapino, G. Manzo, and C. Cannas. Dialkylamide as both capping agent and surfactant in a direct solvothermal synthesis of

magnetite and titania nanoparticles. *Cryst. Growth Des.*, 15(5):2364–2372, 2015.

[72] M. Chen, Y.G. Feng, X. Wang, T.C. Li, J.Y. Zhang, and D.J. Qian. Silver nanoparticles capped by oleylamine: Formation, growth, and self-organization. *Langmuir*, 23:5296–5304, 2007.

[73] N. Shukla, C. Liu, P.M. Jones, and D. Weller. FTIR study of surfactant bonding to FePt nanoparticles. *Journal of Magnetism and Magnetic Materials*, 266:178–184, 2003.

[74] J.W. Thomson, K. Nagashima, P.M. Macdonald, and G.A. Ozin. From sulfur-amine solutions to metal sulfide nanocrystals: Peering into the oleylamine-sulfur black box. *J. Am. Chem. Soc.*, 133:5036–5041, 2011.

[75] E.T. Kim, W.J. Chung, J. Lim, P. Johe, R.S. Glass, J. Pyunb, and K. Char. One-pot synthesis of PbS NP/sulfur-oleylamine copolymer nanocomposites via the copolymerization of elemental sulfur with oleylamine. *Polym. Chem.*, 5:3617, 2014.

[76] B. Xue, T. Sun, F. Mao, and J. Xie. Gelatin-assisted green synthesis of bismuth sulfide nanorods under microwave irradiation. *Materials Letters*, 122:106–109, 2014.

[77] M. Salavati-Niasari, Z. Behfard, and O. Amiri. Synthesis of bismuth sulfide nanostructures by using bismuth(III) monosalicylate precursor and fabrication of bismuth sulfide based p-n junction solar cells. *Asia-Pac. J. Chem. Eng.*, 9:16–23, 2014.

[78] D. Tiwari, D.J. Fermin, T.K. Chaudhuri, and A. Ray. Solution processed bismuth ferrite thin films for all-oxide solar photovoltaics. *J. Phys. Chem. C*, 119:5872–5877, 215.

[79] T. Thongtem, J. Jaroenchaichana, and S. Thongtem. Cyclic microwave-assisted synthesis of flower-like and hexapod silver bismuth sulfide. *Materials Letters*, 63:2163–2166, 2009.

[80] R. Suarez, P.K. Nair, and P.V. Kamat. Photoelectrochemical behavior of Bi_2S_3 nanoclusters and nanostructured thin films. *Langmuir*, 14:3236–3241, 1998.

[81] Jenny Nelson. *Physics of solar cells.* Imperial College Press, 2003.

[82] J C. Blakesley and D. Neher. Relationship between energetic disorder and open-circuit voltage in bulk heterojunction organic solar cells. *Physical Review B*, 84(075210), 2011.

[83] S.N.F. Mohd-Nasir, M.Y. Sulaiman, N. Ahmad-Ludin, M.A. Ibrahim, K. Sopian, and M.A. Mat-Teridi. Review of polymer, dye-sensitized, and hybrid solar cells. *International Journal of Photoenergy*, 2014.

[84] S. Lattante. Electron and hole transport layers: Their use in inverted bulk heterojunction polymer solar cells. *Electronics*, 3:132–164, 2014.

[85] H. Oh, J. Krantz, I. Litzov, T. Stubhan, L. Pinna, and C. Brabec. Comparison of various sol-gel derived metal oxide layers for inverted organic solar cells. *Solar Energy Materials & Solar Cells*, 95:2194–2199, 2011.

[86] D. Shi, V. Adinolfi, R. Comin, M. Yuan, E.i Alarousu, A. Buin, Y. Chen, S. Hoogland, A. Rothenberger, K. Katsiev, Y. Losovyj, X. Zhang, P. A. Dowben, O. F. Mohammed, E.H. Sargent, and O.M. Bakr. Low trap-state density and long carrier diffusion in organolead trihalide perovskite single crystals. *Science*, 347(519):pages, 2015.

[87] D.A.H. Hanaor, I. Chironi, I. Karatchevtseva, G. Triani, and C.C. Sorrell. Single- and mixed-phase TiO_2 powders prepared by excess-

hydrolysis of a titanium alkoxide. *Advances in Applied Ceramics*, 111(3):149–158, 2012.

[88] R. Anedda, C. Cannas, A. Musinu, G. Pinna, G. Piccaluga, and M. Casu. A two-stage citric acid-sol/gel synthesis of ZnO/SiO_2 nanocomposites: study of precursors and final products. *J Nanopart Res*, 10:107–120, 2008.

[89] C. Jeffrey Brinker and G.W. Scherer. *Sol-Gel Science: The Physics and Chemistry of Sol-Gel.* Processing Academic Press, 1990.

[90] M. Niederberger and N. Pinna. *Metal Oxide Nanoparticles in Organic Solvents Synthesis, Formation, Assembly and Application.* Springer, 2009.

[91] R.S. Mane, J.D. Desai, O.-S. Joo, and S.-H. Han. Surface morphology and optical studies of non-aqueous Bi_2S_3 thin films. *Int. J. Electrochem. Sci.*, 2:141–148, 2007.

[92] I. Litzov and C.J. Brabec. Development of efficient and stable inverted bulk heterojunction (BHJ) solar cells using different metal oxide interfaces. *Materials*, 6:5796–5820, 2013.

[93] C.E. Morosanu and G. Siddall. *Thin Films by Chemical Vapour Deposition.* Elsevier, 1990.

[94] Q. Chen, H. Zhou, Z. Hong, S. Luo, H.S. Duan, H.H. Wang, Y. Liu, G. Li, and Y. Yang. Planar heterojunction perovskite solar cells via vapor-assisted solution process. *J. Am. Chem. Soc.*, 136(2):622–625, 2014.

[95] E. Ahlswede, J. Hanisch, and M. Powalla. Comparative study of the

influence of LiF, NaF, and KF on the performance of polymer bulk heterojunction solar cells. *Applied Physics Letters*, 90(163504), 2007.

[96] R. Plass, S. Pelet, J. Krueger, and M. Grätzel. Quantum dot sensitization of organic-inorganic hybrid solar cells. *J. Phys. Chem. B*, 106:7578–7580, 2002.

[97] Y. Song, S. Lv, X. Liu, X. Li, S. Wang, H. Wei, D. Li, Y. Xiao, and Q. Meng. Energy level tuning of TPB-based hole-transporting materials for highly efficient perovskite solar cells. *Chem. Commun.*, 50:15239, 2014.

[98] M. Bernechea, Y. Cao, and G. Konstantatos. Size and bandgap tunability in Bi_2S_3 colloidal nanocrystals and its effect in solution processed solar cells. *J. Mater. Chem. A*, 3:20642–20648, 2015.

[99] V. Shrotriya, J. Ouyang, R.J. Tseng, G. Li, and Y. Yang. Absorption spectra modification in poly(3-hexylthiophene):methanofullerene blend thin films. *Chemical Physics Letters*, 411:138–143, 2015.

[100] C. Borriello, A. Bruno, R. Diana, T. Di Luccio, P. Morvillo, R. Ricciardi, F. Villani, and C. Minarini. PbS nanocrystals in hybrid systems for solar cell applications. *Phys. Status Solidi A*, 212(2):245–251, 2015.

[101] M. Kröger, S. Hamwib, J. Meyer, T. Riedl, W. Kowalsky, and A. Kahn. P-type doping of organic wide band gap materials by transition metal oxides: A case-study on molybdenum trioxide. *Organic Electronics*, 10:932–938, 2009.

[102] C. Girotto, E. Voroshazi, D. Cheyns, Paul Heremans, and B.P. Rand. Solution-processed MoO_3 thin films as a hole-injection layer for organic solar cells. *ACS Appl. Mater. Interfaces*, 3:3244–3247, 2011.

[103] F. Maldonado and A. Stashans. Al-doped ZnO:electronic,electrical and structural properties. *Journal of Physics and Chemistry of Solids*, 71:784–787, 2010.

[104] H. Oh, J. Krantz, I. Litzovand T. Stubhan, L. Pinna, and C.J. Brabec. Comparison of various sol-gel derived metal oxide layers for inverted organic solar cells. *Solar Energy Materials & Solar Cells*, 95:2194–2199, 2011.

[105] A. Kojima, K. Teshima, Y. Shirai, and T. Miyasaka. Organometal halide perovskites as visible-light sensitizers for photovoltaic cells. *J. Am. Chem. Soc.*, 131:6050–6051, 2009.

[106] S. Collavini, S.F. Völker, and J.L. Delgado. Understanding the outstanding power conversion efficiency of perovskite-based solar cells. *Angew. Chem. Int.*, 54:9757–9759, 2005.

[107] G.H. Carey, A.L. Abdelhady, Z. Ning, S.M. Thon, O.M. Bakr, and E.H. Sargent. Colloidal quantum dot solar cells. *Chem. Rev.*, 2015.

[108] Z. Ning, O. Voznyy, J. Pan, S. Hoogland, V. Adinolfi, J. Xu, M. Li, A.R. Kirmani, J.P. Sun, J. Minor, K.W. Kemp, H. Dong, L. Rollny, A. Labelle, G. Carey, B. Sutherland, I. Hill, A. Amassian, H. Liu, J. Tang, O.M. Bakr, and E.H. Sargent. Air-stable n-type colloidal quantum dot solids. *Nat. Mater.*, 13:822–828, 2014.

Acknowledgements

Eccoci finalmente giunti ai ringraziamenti. È piuttosto difficile trovare le parole adatte ad esprimere l'esatto livello di gratitudine che ho verso tutti coloro che mi hanno sostenuto durante questo viaggio durato 3 anni, lungo e breve allo stesso tempo. Per questo motivo, mi prendo la libertà di scriverli in italiano in modo tale da lasciarmi la massima libertà di scrittura, secondo il mio stile. Spero di non dimenticare nessuno perché siete davvero tanti!

Comincio col ringraziare il Prof. Michele Saba per l'opportunità, gli insegnamenti, l'aiuto e la fiducia ricevuti, senza i quali questo dottorato non sarebbe mai arrivato. Questa è stata un'esperienza di crescita personale oltre che professionale e te ne sono grato.

Ringrazio la Prof.ssa Anna Musinu, che ho avuto il piacere di conoscere sin dal mio primo anno di università e con la quale ho potuto collaborare fino ad oggi. Beata la sua pazienza per avermi sopportato così a lungo.

Ringrazio il Prof. Giovanni Bongiovanni, Prof. Andrea Mura, Prof. Francesco Quochi per i consigli e gli insegnamenti ricevuti. Ringrazio la Prof.ssa Carla Cannas, Prof. Mariano Casu, Prof. Guido Ennas e il Dr. Andrea Ardu per avermi permesso di frequentare i vostri laboratori, avermi aiutato con le procedure di laboratorio e per gli innumerevoli consigli ed insegnamenti. Ringrazio inoltre il Dr. Alessandro Mattoni e Vasco per l'importante collaborazione e Mauro, Cristiana e Marina per l'amicizia e i consigli.

Un immenso grazie alla Dott.ssa Daniela Marongiu per la preziosa collab-

orazione, l'amicizia e le risate. Il mio lavoro qui e persino questa tesi non sarebbero stati lo stesso senza il tuo aiuto. I would love to thank my colleague, example and friend Dr. Feipeng Chen for his help in the experiments, the precious discussions and the so many laughs. It was a pleasure to share this experience with both of you.

Un profondo grazie lo rivolgo ai miei carissimi colleghi e amici Barbara, Tommaso, Roberto (il nostro primo ufficio resterà sempre il migliore), Giuliana, Laura, Luigi e Michele. Cominciare questo percorso e condividerlo con voi è stato un onore quanto lo sarà concluderlo insieme. Devo ringraziare nuovamente Michele insieme a Valerio e Nicola, per le chiacchierate scientifiche e non, le risate e le scemate. Questo umile chimico terrorista ha apprezzato ogni minuto.

Ringrazio gli amici conosciuti durante gli studi e con cui ho avuto modo di condividere anche quest'avventura, Valentina (anche stavolta si conclude insieme, visto?), Mauro, Giuseppe, Claudio, Federica T., Marianna, Matteo S., Matteo A. ed Elisa. Sempre gentili, sempre geniali. E grazie anche a Federica O., Sara e Francesca, le migliori artiste pazze che potessi incontrare!

Tornando in ambito universitario e per non fare un torto a nessuno, dato che siete davvero tanti, ringrazio tutti coloro che ho incontrato da quando frequento questo dipartimento. Che vi siate fermati per tanto o poco tempo, anche solo il tempo di un pranzo o un caffé insieme, o che siate venuti da ogni angolo di mondo, o che parliate una lingua che neanche capisco, è stato un piacere conoscervi.

Un ringraziamento speciale va a tutti i laureandi che ho seguito durante le loro attività in laboratorio e che ho visto infine laurearsi e agli studenti del primo anno della laurea triennale di Fisica a cui ho fatto da tutor in questi tre anni. Vi ringrazio perché, forse non lo avrete notato, ma anche io ho imparato molto da voi.

Voglio ringraziare per ultima, ma non certo per importanza, la mia famiglia per avermi sempre sostenuto nonostante i problemi di ogni giorno, sopportando i miei sproloqui scientifici anche senza capirli. Grazie.

Dedico questo lavoro ai pazzi, siano essi scienziati o artisti, che non mollano mai nonostante vada tutto storto. E dedico questa tesi a quel sorriso, che fu luce nel buio.